J|A|C|S
ARTICLES
Published on Web 12/21/2001

Spectroscopic Studies of *Pyrococcus furiosus* Superoxide Reductase: Implications for Active-Site Structures and the Catalytic Mechanism

Michael D. Clay,[†] Francis E. Jenney, Jr.,[‡] Peter L. Hagedoorn,[†,§] Graham N. George,[||] Michael W. W. Adams,[‡] and Michael K. Johnson*[,†]

Contribution from the Departments of Chemistry and Biochemistry & Molecular Biology, and the Center for Metalloenzyme Studies, University of Georgia, Athens, Georgia 30602, and Stanford Synchrotron Radiation Laboratory, SLAC, Stanford University, P.O. Box 4349, MS 69, Stanford, California 94309

Received August 20, 2001

Abstract: The combination of UV/visible/NIR absorption, CD and variable-temperature magnetic circular dichroism (VTMCD), EPR, and X-ray absorption (XAS) spectroscopies has been used to investigate the electronic and structural properties of the oxidized and reduced forms of *Pyrococcus furiosus* superoxide reductase (SOR) as a function of pH and exogenous ligand binding. XAS shows that the mononuclear ferric center in the oxidized enzyme is very susceptible to photoreduction in the X-ray beam. This observation facilitates interpretation of ground- and excited-state electronic properties and the EXAFS results for the oxidized enzyme in terms of the published X-ray crystallographic data (Yeh, A. P.; Hu, Y.; Jenney, F. E.; Adams, M. W. W.; Rees, D. C. *Biochemistry* **2000**, *39*, 2499−2508). In the oxidized state, the mononuclear ferric active site has octahedral coordination with four equatorial histidyl ligands and axial cysteinate and monodentate glutamate ligands. Fe EXAFS are best fit by one Fe−S at 2.36 Å and five Fe−N/O at an average distance of 2.12 Å. The EPR-determined spin Hamiltonian parameters for the high-spin ($S = {}^5/_2$) ferric site in the resting enzyme, $D = -0.50 \pm 0.05$ cm^{-1} and $E/D = 0.06$, are consistent with tetragonally compressed octahedral coordination geometry. UV/visible absorption and VTMCD studies facilitate resolution and assignment of πHis → Fe^{3+}(t_{2g}) and (Cys)S(p) → Fe^{3+}(t_{2g}) charge-transfer transitions, and the polarizations deduced from MCD saturation magnetization studies indicate that the zero-field splitting (compression) axis corresponds to one of the axes with *trans*-histidyl ligands. EPR and VTMCD studies provide evidence of azide, ferrocyanide, hydroxide, and cyanide binding via displacement of the glutamate ligand. For azide, ferrocyanide, and hydroxide, ligand binding occurs with retention of the high-spin ($S = {}^5/_2$) ground state ($E/D = 0.27$ and $D < 0$ for azide and ferrocyanide; $E/D = 0.25$ and $D = +1.1 \pm 0.2$ cm^{-1} for hydroxide), whereas cyanide binding results in a low-spin ($S = {}^1/_2$) species ($g = 2.29, 2.25, 1.94$). The ground-state and charge-transfer/ligand-field excited-state properties of the low-spin cyanide-bound derivative are shown to be consistent with a tetragonally elongated octahedral coordination with the elongation axis corresponding to an axis with *trans*-histidyl ligands. In the reduced state, the ferrous site of SOR is shown to have square-pyramidal coordination geometry in frozen solution with four equatorial histidines and one axial cysteine on the basis of XAS and UV and NIR VTMCD studies. Fe EXAFS are best fit by one Fe−S at 2.37 Å and four Fe−N/O at an average distance of 2.15 Å. VTMCD reveals a high-spin ($S = 2$) ferrous site with (Cys)S(p) → Fe^{2+} charge-transfer transitions in the UV region and $^5T_{2g} \rightarrow {}^5E_g$ ligand-field transitions in the NIR region at 12400 and <5000 cm^{-1}. The ligand-field bands indicate square-pyramidal coordination geometry with $10Dq < 8700$ cm^{-1} and a large excited-state splitting, $\Delta^5E_g > 7400$ cm^{-1}. Analysis of MCD saturation magnetization data leads to ground-state zero-field splitting parameters for the $S = 2$ ground state, $D \sim +10$ cm^{-1} and $E/D \sim 0.1$, and complete assessment of ferrous d-orbital splitting. Azide binds weakly at the vacant coordination site of reduced SOR to give a coordination geometry intermediate between octahedral and square pyramidal with $10Dq = 9700$ cm^{-1} and $\Delta^5E_g = 4800$ cm^{-1}. Cyanide binding results in an octahedral ferrous site with $10Dq = 10\,900$ cm^{-1} and $\Delta^5E_g = 1750$ cm^{-1}. The ability to bind exogenous ligands to both the ferrous and ferric sites of SOR is consistent with an inner-sphere catalytic mechanism involving superoxide binding at the ferrous site to yield a ferric−(hydro)peroxo intermediate. The structural and electronic properties of the SOR active site are discussed in relation to the role and bonding of the axial cysteine residue and the recent proposals for the catalytic mechanism.

Introduction

Over the last three years, evidence has emerged for a novel mechanism of oxygen detoxification in anaerobic and microaerophilic microorganisms involving an enzyme that preferentially catalyzes superoxide reduction rather than superoxide dismutation.[1−5] Superoxide reductase (SOR) is proposed to

* To whom correspondence should be addressed: (telephone) 706-542-9378; (fax) 706-542-2353; (e-mail) johnson@sunchem.chem.uga.edu.
[†] Department of Chemistry and the Center for Metalloenzyme Studies, University of Georgia.
[‡] Department of Biochemistry & Molecular Biology and the Center for Metalloenzyme Studies, University of Georgia.
[§] Present address: Department of Biotechnology, Technical University of Delft, The Netherlands.
[||] Stanford University.

10.1021/ja016889g CCC: $22.00

catalyze the reduction of superoxide to hydrogen peroxide utilizing electrons from NADPH, by way of NADPH: rubredoxin oxidoreductase and rubredoxin.[2] In anaerobic or microaerophilic organisms, SOR may offer a selective advantage over superoxide dismutase (SOD) for removing superoxide, by eliminating the concomitant generation of O_2.[2]

Thus far, three distinct types of enzymes with superoxide reductase activity have been characterized. The initial evidence for an enzyme with superoxide reductase activity came from the hyperthermophilic anaerobe *Pyrococcus furiosus*.[2] The superoxide reductase activity was associated with a heterotetramer composed of 14.3-kDa subunits, each containing a single non-heme iron. This protein was shown to be homologous (50% identity) with neelaredoxin from *Desulfovibrio gigas*; a spectroscopically characterized non-heme iron protein[6] that had previously been reported to have significant SOD activity.[7] The structures of oxidized and reduced forms of *P. furiosus* SOR have been determined at 1.7- and 2.0-Å resolution, respectively,[8] and the protein fold and iron center were found to be very similar to a homologous domain in *Desulfovibrio desulfuricans* desulfoferrodoxin (Dfx).[9] Desulfoferrodoxins have been purified and characterized from many sulfate-reducing bacteria and are known to be modular non-heme iron proteins comprising a rubredoxin-like desulforedoxin domain and a neelaredoxin-like domain.[10−12] While initial studies of *D. desulfuricans* Dfx indicated SOD activity,[13] more recent studies of *Desulfoarculus baarsii* and *Desulfovibrio vulgaris* Dfx have provide strong evidence that this protein also functions as a superoxide reductase.[3,14] Most recently, an enzyme with superoxide reductase activity has been purified and characterized from *Treponema pallidum*, a microaerophilic bacterium responsible for venereal syphilis that lacks the classical antioxidant enzymes found in aerobic organisms.[4,5] *T. pallidum* SOR has strong sequence homology to Dfx but lacks three of the cysteine residues that ligate the rubredoxin-like iron center in the desulforedoxin domain.

The X-ray structures *P. furiosus* SOR and *D. desulfuricans* Dfx reveal a novel SOR active site involving a mononuclear iron coordinated by the imidazole nitrogens of four histidines (three ϵN and one δN) in a planar arrangement, with a cysteinyl sulfur occupying one axial position.[8,9] There is currently no clear consensus concerning a sixth ligand in the oxidized state. In two of the four subunits of *P. furiosus* SOR, a conserved glutamate carboxylate serves as an axial ligand to form a six-coordinate, octahedral environment.[8] In the other two subunits of *P. furiosus* SOR,[8] and in *D. desulfuricans* Dfx,[9] the sixth coordination site is either vacant or occupied by a solvent molecule. A similar five-coordinate square-pyramidal iron site is present in reduced *P. furiosus* SOR.[8] Hence, the possibility of partial or complete reduction during crystallization or photoreduction in the X-ray beam may provide an explanation of the apparent variability in the oxidized active-site structure.[8]

P. furiosus SOR is anomalous among metalloenzymes in that X-ray structure determination has preceded detailed spectroscopic analysis. To address the active-site geometric and electronic structure in solution and the origin of the heterogeneity apparent in the oxidized crystal structure, we report here the results of EPR, UV/visible/near-IR absorption, CD, and variable-field/variable-temperature magnetic circular dichroism (VHVT MCD), and X-ray absorption (XAS) studies of the oxidized and reduced forms of native and recombinant forms of *P. furiosus* SOR, as a function of pH and the binding of exogenous ligands. The results provide the first detailed assessment of the ground- and excited-state properties of the mononuclear Fe active site of SOR in both the oxidized and reduced states and provide evidence for binding of cyanide and azide at the active site in both oxidation states. In addition, the spectroscopic results address the origin of the conflicting reports concerning the ground-state properties of the high-spin Fe^{3+} center in oxidized SOR and Dfx samples[3−6,10−12,15] and provide assessment of metrical data for Fe−ligand distances in solution. The exogenous ligand binding properties and the spectroscopically determined Fe^{3+} and Fe^{2+} coordination geometries and excited-state properties are discussed in relation to the role and bonding of the axial cysteine residue and the recent proposals for the catalytic mechanism.[14,16,17]

Experimental Section

Cloning of the *P. furiosus sor* Gene. All standard molecular biology techniques were performed using the published protocols.[18] *P. furiosus* cells (DSM 3638) were grown and cell-free extracts were prepared as previously described.[19] The gene encoding *P. furiosus* SOR (*sor*) was cloned into the expression vector pET3a (Novagen, Madison, WI) and designated pPfNd1. *Escherichia coli* strain BL21(DE3) was used for expression of recombinant *P. furiosus* SOR and was grown in a 100-L fermenter at 37 °C stirred at 170 rpm under aerobic conditions in M9 minimal medium[18] supplemented with 0.4% glycerol as carbon source, 100 μM $FeSO_4$, 0.05% thiamine, 1× vitamins,[20] and 200 μg/mL ampicillin in a 100-L fermenter. Cultures were then grown to $A_{600} \sim 0.7$ and induced with 1 mM IPTG for 4 h.

Purification of Recombinant *P. furiosus* SOR. Frozen *E. coli* cells (116 g) were thawed (1 g/3 mL) in 50 mM Tris-HCl buffer (pH 8.5)

(1) Liochev, S. I.; Fridovich, I. *J. Biol. Chem.* **1997**, *272*, 25573−25575.
(2) Jenney, F. E.; Verhagen, M. F. J. M.; Cui, X.; Adams, M. W. W. *Science* **1999**, *286*, 306−309.
(3) Lombard, M.; Fontecave, M.; Touati, D.; Nivière, V. *J. Biol. Chem.* **2000**, *275*, 115−121.
(4) Lombard, M.; Touati, D.; Fontecave, M.; Nivière, V. *J. Biol. Chem.* **2000**, *275*, 27021−27026.
(5) Jovanovi'c, T.; Ascenso, C.; Hazlett, K. R. O.; Sikkink, R.; Krebs, C.; Litwiller, L. M.; Benson, L. M.; Moura, I.; Moura, J. J. G.; Radolf, J. D.; Huynh, B. H.; Naylor, S.; Rusnak, F. M. *J. Biol. Chem.* **2000**, *275*, 28439−28448.
(6) Chen, L.; Sharma, P.; LeGall, J.; Mariano, A. M.; Teixeira, M.; Xavier, A. V. *Eur. J. Biochem.* **1994**, *226*, 613−618.
(7) Silva, G.; Oliveira, S.; Gomes, C. M.; Pacheco, I.; Liu, M.-Y.; Xavier, A. V.; Teixeira, M.; LeGall, J.; Rodrigues-Pousada, C. *Eur. J. Biochem.* **1999**, *259*, 235−243.
(8) Yeh, A. P.; Hu, Y.; Jenney, F. E.; Adams, M. W. W.; Rees, D. C. *Biochemistry* **2000**, *39*, 2499−2508.
(9) Coelho, A. V.; Matias, P.; Fülöp, V.; Thompson, A.; Gonzalez, A.; Carrondo, M. A. *J. Biol. Inorg. Chem.* **1997**, *2*, 680−689.
(10) Moura, I.; Tavares, P.; Moura, J. J. G.; Ravi, N.; Huynh, B. H.; Liu, M.-Y.; LeGall, J. *J. Biol. Chem.* **1990**, *265*, 21596−21602.
(11) Tavares, P.; Ravi, N.; Moura, J. J. G.; LeGall, J.; Huang, Y.-H.; Crouse, B. R.; Johnson, M. K.; Huynh, B. H.; Moura, I. *J. Biol. Chem.* **1994**, *269*, 10504−10510.
(12) Ascenso, C.; Rusnak, F. M.; Cabrito, I.; Lima, M. J.; Naylor, S.; Moura, I.; Moura, J. J. G. *J. Biol. Inorg. Chem.* **2000**, *5*, 720−729.
(13) Romão, C. V.; Liu, M.-Y.; LeGall, J.; Gomes, C. M.; Braga, V.; Pacheco, I.; Xavier, A. V.; Teixeira, M. *Eur.J. Biochem.* **1999**, *261*, 438−443.
(14) Coulter, E. D.; Emerson, J. P.; Kurtz, D. M., Jr.; Cabelli, D. E. *J. Am. Chem. Soc.* **2000**, *122*, 11555−11556.
(15) Verhagen, M. F. J. M.; Voorhorst, W. G. B.; Kolkman, J. A.; Wolbert, R. B. G.; Hagen, W. R. *FEBS Lett.* **1993**, *336*, 13−18.
(16) Lombard, M.; Houée-Levin, C.; Touati, D.; Fontecave, M.; Nivière, V. *Biochemistry* **2001**, *40*, 5032−5040.
(17) Nivière, V.; Lombard, M.; Fontecave, M.; Houée-Levin, C. *FEBS Lett.* **2001**, *497*, 171−173.
(18) Sambrook, J.; Fritsch, E. F.; Maniatis, T. *Molecular Cloning: A Laboratory Manual*, 2nd ed.; Cold Spring Harbor Laboratory Press: Cold Spring Harbor, NY, 1998.
(19) Bryant, F. O.; Adams, M. W. W. *J. Biol. Chem.* **1989**, *264*, 5070−5079.
(20) Venters, R. A.; Calderone, T. L.; Spicer, L. D.; Fierke, C. A. *Biochemistry* **1991**, *30*, 4491−4494.

containing 1 mM EDTA, 0.5 mg/mL lysozyme, 100 mM NaCl, and 1 mM phenylmethanesulfonyl fluoride. The cells were broken at 4 °C by sonication, and the extract was heated until the solution temperature reached 70 °C and then chilled on ice for 2 h. After centrifugation (25000*g*, 45 min, 4 °C), the supernatant (460 mL, 920 mg of protein) was applied, diluted by 75% with buffer, to a column of Q Sepharose FastFlow equilibrated with 50 mM Tris-HCl (pH 8.5). A linear gradient from 0 to 75 mM NaCl was applied followed by a linear gradient from 75 to 500 mM NaCl. Fractions containing SOR eluted as 190−250 mM NaCl was applied. These were concentrated by ultrafiltration, ammonium sulfate was added to a final concentration of 1 M, and this sample was applied to a column of Phenyl Sepharose equilibrated in 20 mM MOPS (pH 7.0) containing 1 M $(NH_4)_2SO_4$. SOR was block eluted with 20 mM MOPS (pH 7.0), concentrated, and desalted by ultrafiltration. The final yield was 131 mg of SOR from 116 g of *E. coli* cells wet weight.

Biochemical Techniques and Sample Preparation. Protein concentrations were measured using the Biuret method after trichloroacetic acid (TCA) precipitation,[21] except that samples were heated at 50 °C for 30 min after TCA addition. The superoxide reductase activity of SOR and its apparent SOD activity were measured as previously described.[2] Superoxide reductase activity was measured as the difference in the rate of cytochrome *c* reduction with and without SOR. One unit of activity catalyzes the reduction of 1 μmol of superoxide/min, which is equivalent to 1 μmol of cytochrome oxidized/min. Calculations of the superoxide reductase activity of SOR assume negligible SOD activity.[2] Iron reconstitution of native *P. furiosus* SOR was performed in sealed vials under argon. The conditions were as follows: 50 mM Tris-HCl (pH 8.0), 0.5 mM protein, 100 mM dithiothreitol, and 10 mM $Fe(NH_4)_2SO_4$, for 30 min at 25 °C followed by 30 min at 80 °C. The samples were then desalted using a Sephadex G25 column in 50 mM Tris-HCl (pH 8) and concentrated by ultrafiltration.

Buffer exchange prior to spectroscopic measurements was carried out by ultrafiltration, and the buffering media used for individual samples are indicated in the figure legends. Stock solutions of potassium cyanide or sodium azide were freshly prepared in the same buffers as the samples. Reduction of SOR was carried out under anaerobic conditions by addition of a 10-fold stoichiometric excess of dithionite or ascorbate. Excess reductant was removed by ultrafiltration prior to addition of azide or cyanide and subsequent spectroscopic studies. All reduced samples were handled in a Vacuum Atmospheres glovebox (<1 ppm O_2).

Spectroscopic Methods. XAS measurements were carried out at the Stanford Synchrotron Radiation Laboratory with the SPEAR storage ring containing 60−100 mA at 3.0 GeV. Data were collected on beam line 7-3 using a Si(220) double-crystal monochromator, with an upstream vertical aperture of 1 mm, and a wiggler field of 1.8 T. Harmonic rejection was accomplished by detuning one monochromator crystal to ~50% off peak, and no specular optics were present in the beam line. The incident X-ray intensity was monitored using a nitrogen-filled ionization chamber and X-ray absorption was measured as the X-ray Fe Kα fluorescence excitation spectrum using an array of 13 germanium intrinsic detectors.[22] During data collection, samples were maintained at a temperature of ~10 K, using an Oxford Instruments liquid helium flow cryostat. For each sample, 8−10 35-min scans were accumulated, and the absorption of an iron metal foil was measured simultaneously by transmittance. For the oxidized enzyme, the sample position was adjusted after each scan in order to illuminate a fresh part of the sample and to prevent photoreduction. The X-ray energy was calibrated with reference to the lowest energy inflection point of the foil, which was assumed to be 7111.3 eV. The extended X-ray absorption fine structure (EXAFS) oscillations $\chi(k)$ were quantitatively analyzed by curve-fitting the weighted *k*-space data using the EXAFSPAK suite of computer programs,[23] employing ab initio theoretical phase and amplitude functions generated with the program FEFF version 8.2.[24] No smoothing, Fourier filtering, or related manipulations were performed upon the data.

Absorption spectra were recorded on Shimadzu UV301PC spectrophotometer. VHVT MCD measurements were recorded on samples containing 55% (v/v) glycerol or glycerol-d_3 using a Jasco J-715 (180−1000 nm) or J-730 (700−2000 nm) spectropolarimeter mated to an Oxford Instruments Spectromag 4000 (0−7 T) split-coil superconducting magnet. The experimental protocols for measuring MCD spectra of oxygen-sensitive samples over the temperature range 1.5−300 K with magnetic fields up to 7 T have been described elsewhere.[25] VHVT MCD saturation magnetization data for the high-spin ($S = {}^5/_2$) Fe^{3+} and high-spin ($S = 2$) Fe^{2+} species were analyzed according to the published procedures,[26,27] using software kindly supplied by Professor Edward I. Solomon and Dr. Frank Neese. X-band (~9.6 GHz) EPR spectra were recorded on a Bruker ESP-300E EPR spectrometer with a dual-mode ER-4116 cavity and equipped with an Oxford Instruments ESR-9 flow cryostat (4.2−300 K). Frequencies were measured with a Hewlett-Packard 5350B frequency counter, and the field was calibrated with a Bruker ER 035M gaussmeter. EPR spin quantitations based on the total area under the absorption envelope or the area under the low-field "absorption-shaped" feature in the first-derivative spectrum were carried out using the procedures developed by Aasa and Vänngård.[28] Simulations of $S = {}^1/_2$ signals were carried out using the Simfonia software package (Bruker Instruments).

EPR redox titrations were performed at ambient temperature (25−27 °C) in the glovebox under anaerobic conditions using 300 μM SOR in a 100 mM HEPES buffer (pH 7.5). Mediator dyes were added, each to a concentration of ~60 μM, to cover the desired range of redox potentials: i.e., 1,4-benzoquinone, 1,2-naphthoquinone, thionine, methylene blue, duroquinone, and 1,2-naphthoquinone-4-sulfonate. Samples were first oxidized with a minimal excess of potassium ferricyanide followed by reductive titration with ascorbate. After equilibration at the desired potential, a 0.2-mL aliquot was transferred to a calibrated EPR tube and immediately frozen in liquid nitrogen. Potentials were measured using a platinum working electrode and a saturated Ag/AgCl reference electrode. All redox potentials are reported relative to NHE.

Results and Analysis

EPR. X-band EPR was not effective in probing the ground-state properties of the Fe^{2+} center in ascorbate-reduced *P. furiosus* SOR. No resonances indicative of an integer spin species were observed over the temperature range 4.2−100 K in either parallel or perpendicular mode. The ground-state properties of the Fe^{3+} center in oxidized *P. furiosus* SOR were investigated by EPR as a function of pH and the addition of excess cyanide and azide (Figure 1). As prepared in pH 7.5 HEPES buffer, the EPR spectrum of *P. furiosus* SOR (Figure 1A) is composed of two overlapping $S = {}^5/_2$ resonances and the effective *g*-values of each are readily rationalized using an isotropic $S = {}^5/_2$ spin Hamiltonian of the form

(21) (a) Goa, J. *Scand. J. Clin. Lab. Invest.* **1953**, *5*, 218−222. (b) Bensadoun, A.; Weinstein, D. *Anal. Biochem.* **1976**, *70*, 241−250.
(22) Cramer, S. P.; Tench, O.; Yocum, M.; George, G. N. *Nucl. Instrum. Methods Phys. Res.* **1998**, *A266*, 586−591.
(23) (a) http://ssrl.slac.stanford.edu/exafspak.html. (b) George, G. N.; Garrett, R. M.; Prince, R. C.; Rajagopalan, K. V. *J. Am. Chem. Soc.* **1996**, *118*, 8588−8592.
(24) (a) Rehr, J. J.; Mustre de Leon, J.; Zabinsky, S. I.; Albers, R. C. *J. Am. Chem. Soc.* **1991**, *113*, 5135−5140. (b) Mustre de Leon, J.; Rehr, J. J.; Zabinsky, S. I.; Albers, R. C. *Phys. Rev.* **1991**, *B44*, 4146−4156.
(25) (a) Johnson, M. K. In *Metal Clusters in Proteins*; Que, L., Jr., Ed.; American Chemical Society: Washington, DC, 1988; pp 326−342. (b) Thomson, A. J.; Cheesman, M. R.; George, S. J. *Methods Enzymol.* **1993**, *226*, 199−232.
(26) Neese, F.; Solomon, E. I. *Inorg. Chem.* **1999**, *38*, 1847−1865.
(27) Solomon, E. I.; Pavel, E. G.; Loeb, K. E.; Campochiaro, C. *Coord. Chem. Rev.* **1995**, *144*, 369−460.
(28) Aasa, R.; Vänngård, T. *J. Magn. Reson.* **2000**, *19*, 308−315.

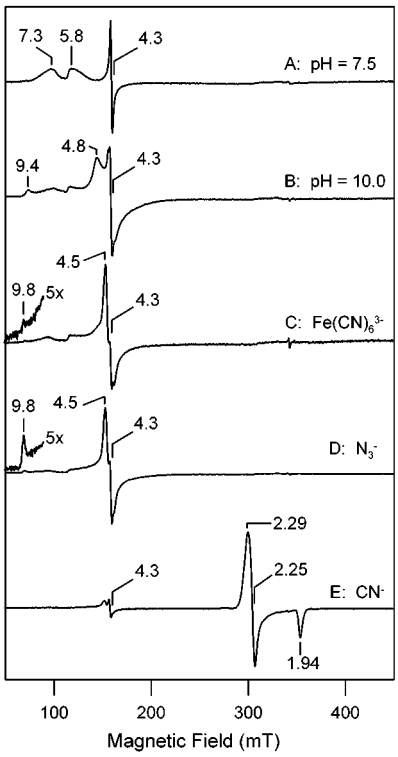

Figure 1. X-band EPR spectra of recombinant *P. furiosus* SOR: (A) 50 mM HEPES buffer (pH 7.5); (B) 100 mM CHES buffer (pH 10.0); (C) sample A after oxidation with a 5-fold excess of ferricyanide and removal of ferricyanide by ultrafiltration; (D) sample A after addition of a 45-fold stoichiometric excess of sodium azide at room temperature; (E) 50 mM Taps buffer (pH 8.5), after addition of a 30-fold stoichiometric excess of sodium cyanide at room temperature. All samples were ~0.5 mM in SOR and all spectra were recorded at 9.60 GHz, using a modulation amplitude of 0.63 mT. The microwave power and temperature were 40 mW and 4.2 K for (A−D) and 1 mW and 15 K for (E). Selected g-values are shown on each spectrum.

$$H_e = g_0\beta\mathbf{H}\cdot\mathbf{S} + D(\mathbf{S}_z^2 - S(S+1)/3) + E(\mathbf{S}_x^2 - \mathbf{S}_y^2) \quad (1)$$

where D and E are the axial and rhombic zero-field splitting parameters, respectively. The major $S = {}^5/_2$ species gives rise to the broad absorption-shaped features centered at $g = 7.3$ and 5.8. On the basis of their temperature-dependence behavior (see Figure 2), the $g = 7.3$ and 5.8 features are attributed to the low-field components of resonances from the upper and middle doublets, respectively, of an axial $S = {}^5/_2$ spin system with $D < 0$. For example, for $D < 0$, $E/D = 0.06$ and a $g_0 = 2$, eq 1 predicts $g_{x,y,z} = (9.99, 0.02, 0.03)$, (5.88, 1.35, 1.43), and (1.89, 7.33, 4.55) for the lower ("$M_s = \pm{}^5/_2$"), middle ("$M_s = \pm{}^3/_2$"), and upper ("$M_s = \pm{}^1/_2$") doublets, respectively. A resonance from the lowest doublet is predicted to have very low transition probability and is observable as a weak absorption-shaped band at $g = 10.0$ in the spectrum recorded at 3.5 K (see Figure 2). For the upper and middle doublets, the components with $g < 2$ are too broad to observe, and a broad derivative centered near $g = 4.5$ from the $M_s = \pm{}^1/_2$ doublet is obscured by the $g = 4.3$ resonance of the minor species. The energy separation between the middle and upper zero-field doublets can be estimated from the slope of a plot of the logarithm of the ratio of the intensity of the two field resonances, $\ln(I_{g=5.8}/I_{g=7.3})$ versus $1/T$, which yields a straight line of slope 1.62 ± 0.10 K. This indicates an energy separation of 1.1 ± 0.1 cm^{-1}, which translates to $D = -0.50 \pm 0.05$ cm^{-1}. The breadth of the $g = 7.3$ and 5.8 features indicates significant E/D strain resulting from conformational heterogeneity in the frozen solution. In accord with the published EPR studies of *D. gigas* neelaredoxin,[6] the line shapes indicate that the heterogeneity primarily involves two species with E/D values close to 0.05 and 0.08. Spin quantitations based on the total integrated area under the absorption-shaped features at $g = 7.3$ and 5.8, using the method developed by Aasa and Vänngård,[28] and allowing for the Boltzmann populations of the upper and middle doublets, respectively, indicate that the axial $S = {}^5/_2$ species accounts for ~80% of the Fe in the sample.

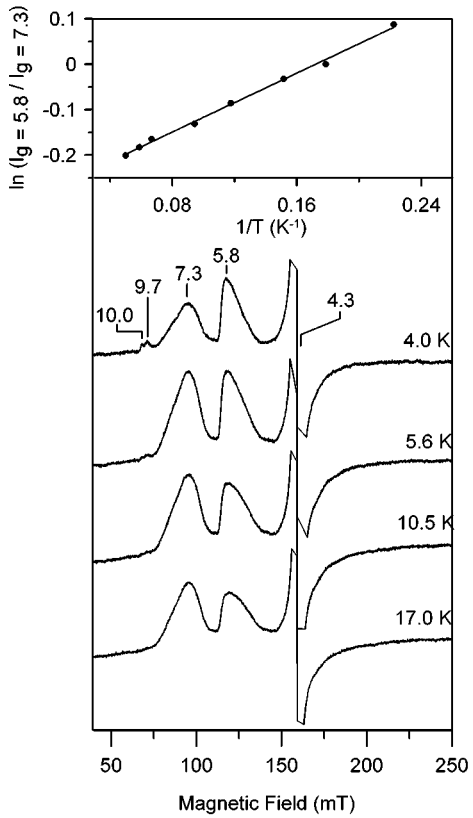

Figure 2. Temperature dependence of the EPR spectrum of recombinant *P. furiosus* SOR in 50 mM HEPES buffer (pH 7.5). The sample and conditions of measurement are as described in Figure 1 except for the temperatures, which are indicated on the spectra. Selected g-values are shown on the 4.0 K spectrum. The inset shows a plot of $\ln(I_{g=5.8}/I_{g=7.3})$ versus $1/T$ which yields a straight line of slope 1.62 ± 0.10 K.

The minor $S = {}^5/_2$ species is responsible for the sharp derivative-shaped feature centered at $g = 4.3$ and a weak absorption-shaped feature at $g = 9.7$ that is only clearly apparent at temperatures of <6 K (see Figures 1 and 2). These resonances are indicative of a rhombic $S = {}^5/_2$ ground state, $E/D = 0.33$, which is predicted to have $g_{x,y,z} = (0.86, 0.61, 9.68)$, (4.29, 4.29, 4.29), and (0.86, 9.68, 0.61) for the lower, middle, and upper doublets, respectively, for $g_0 = 2$. Such resonances are commonly associated with adventitiously bound Fe^{3+} ion. Approximate spin quantitation of the rhombic $S = {}^5/_2$ species by double integration of the $g = 4.3$ component and correcting for the Boltzmann population of the middle doublet using maximal assessments of the zero-field splitting (assuming $|D| < 2$ cm^{-1}), indicates that this species accounts for <10% of the Fe in samples of recombinant *P. furiosus* SOR. The low-spin quantitation, coupled with both the variation in the relative intensities of the axial and rhombic $S = {}^5/_2$ species in *P. furiosus* SOR

and *D. gigas* neelaredoxin,[6] and the much lower redox potential of the species responsible for the rhombic $S = {}^5/_2$ species (see below), are consistent with assignment of this species to adventitious Fe^{3+} ion. However, it has not been possible to decrease the intensity of the rhombic $S = {}^5/_2$ species relative to the axial $S = {}^5/_2$ species in recombinant SOR by treatment with Fe^{3+} chelators such as EDTA, indicating that this adventitious Fe^{3+} ion is tightly bound or not solvent accessible.

Direct evidence that the axial ($E/D = 0.06$) $S = {}^5/_2$ species, rather than the rhombic ($E/D = 0.33$) $S = {}^5/_2$ species, is associated with active enzyme from EPR studies of native *P. furiosus* SOR. As purified, native *P. furiosus* SOR was deficient in Fe (0.4 Fe atoms/subunit) and has very low SOR activity (48 units/mg),[29] compared to the recombinant enzyme (1.0 Fe atoms/subunit and specific activity of 2700 units/mg). However, reconstitution of the native enzyme with excess ferrous ion and repurification yielded samples with increased Fe content (0.7 Fe atoms/subunit) and activity (300 units/mg). The EPR spectra of both the as-prepared and reconstituted samples of native *P. furiosus* SOR (data not shown) were completely dominated by the rhombic ($E/D = 0.33$) $S = {}^5/_2$ species. The axial ($E/D = 0.06$) $S = {}^5/_2$ species was only clearly apparent in the reconstituted sample, but the ratio of the axial and rhombic resonances in this sample was 10-fold less than in the recombinant enzyme. Hence, there appears to be a direct correlation between the axial ($E/D = 0.06$) $S = {}^5/_2$ species and SOR activity.

Dye-mediated EPR redox titrations of recombinant *P. furiosus* SOR using ascorbate as the reductant and ferricyanide as the oxidant revealed an unexpected complication. Oxidation of *P. furiosus* SOR with ferricyanide results in the appearance of a third type of $S = {}^5/_2$ resonance, in addition to the $E/D = 0.06$ and 0.33 species that are also present in the as-prepared samples (Figure 1C). This resonance dominates the EPR spectrum and has a broad derivative centered around $g = 4.3$ with a maximum at $g = 4.5$ and a minimum at $g = 4.2$. In addition, it is associated with a weak absorption feature at $g = 9.8$ which increases in relative intensity with decreasing temperature. These features are readily interpreted in terms of the spin Hamiltonian in eq 1 with $E/D = 0.27$ and $D < 0$. This resonance persists even after excess ferricyanide is removed by ultrafiltration but is not observed in samples oxidized with either hexachloroiridate or hydrogen peroxide. Hence, it appears to be an artifact of ferricyanide oxidation. On the basis of the close similarity to the azide-bound form (see below), this resonance is tentatively attributed to a species with ferrocyanide bound at the Fe^{3+} active site via an Fe−N−C−Fe linkage. EPR-monitored redox titrations facilitated discrimination between the adventitious and active-site Fe^{3+} species. The $E/D = 0.33$ species, corresponding to adventitiously bound Fe^{3+} ion, is not reduced at potentials down to 0 mV, whereas the $E/D = 0.06$ and 0.27 species both exhibit one-electron redox potentials of $+250 \pm 20$ mV (see Figure 3). The EPR-determined redox potential for the $E/D = 0.06$ species in frozen solution is in good agreement with the optically determined redox potential obtained at room temperature, $E_m = +238 \pm 10$ mV (see Supporting Information, Figure S1). However, the ferricyanide-induced species cannot be distinguished from the as-prepared enzyme based on redox potential and, therefore, is easily misinterpreted as arising from the active site of the oxidized resting enzyme.

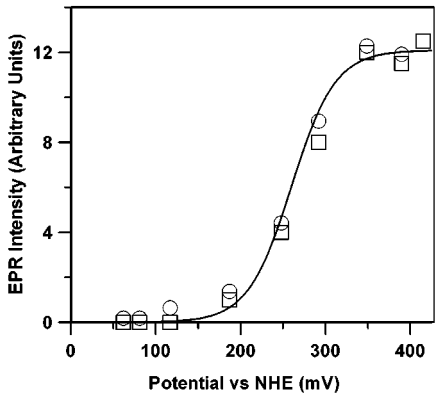

Figure 3. Dye-mediated EPR redox titration of recombinant *P. furiosus* SOR in 50 mM HEPES buffer (pH 7.5). Intensities at $g = 7.3$ (□) and $g = 4.5$ (O) are plotted as a function of redox potential (versus NHE). Samples for EPR were taken at selected poised potentials during ascorbate reduction of the ferricyanide-oxidized enzyme. The solid line is a one-electron Nernst plot with $E_m = +250$ mV.

Optical absorption studies of *D. gigas* neelaredoxin[6] and *P. furiosus* SOR (see Supporting Information, Figure S2) reveal an alkaline transition with a $pK_a = 9.6$. This transition is also evident by the appearance of a new $S = {}^5/_2$ resonance in EPR spectra recorded at pH 10 (Figure 1B). At pH 10, the EPR spectrum has contributions from both the $E/D = 0.06$ and 0.33 species that are present at neutral pH, but samples at higher pH exhibited poorer quality spectra due to progressive loss of Fe at pH values above 10.5. Temperature-dependence studies show that the alkaline form of *P. furiosus* SOR exhibits a broad resonance with a positive feature at $g = 4.8$ and derivative centered near $g = 4.1$ from the middle doublet and a low-field absorption-shaped feature at $g = 9.4$ from the lower doublet (see Figure 4). These effective g-values are readily rationalized by the spin Hamiltonian in eq 1, with $E/D = 0.25$, $D > 0$, and $g_0 = 2$, which predicts $g_{x,y,z} = (0.92, 9.40, 1.45)$, (4.76, 3.76, 4.08), and (9.83, 0.36, 0.47) for the lower, middle, and upper doublets of the $S = {}^5/_2$ zero-field-split manifold, respectively. The energy separation between the middle and lower zero-field doublets was estimated from a plot of $\ln(I_{g=4.8}/I_{g=9.4})$ versus $1/T$, which yields a straight line of slope -4.8 ± 0.4 K (inset in Figure 4), and leads to an estimate of axial zero-field splitting parameter, $D = +1.1 \pm 0.2$ cm^{-1}.

EPR evidence for azide and cyanide binding to the Fe^{3+} active site is shown in Figure 1D and E, respectively. Addition of a 45-fold excess of sodium azide results in the emergence of an $S = {}^5/_2$ resonance indistinguishable from the ferricyanide-induced species, i.e., a broad derivative centered at $g = 4.3$ with a maximum at $g = 4.5$ and a minimum at $g = 4.2$ and low-field absorption-shaped feature at $g = 9.8$. Temperature-dependence studies indicate analogous zero-field splitting parameters; i.e., $E/D = 0.27$ and $D < 0$. Addition of a 30-fold excess of sodium cyanide results in quantitative conversion to a low-spin $S = {}^1/_2$ Fe^{3+} species with near-axial line shape, $g_{1,2,3} = 2.289, 2.251, 1.935$ and line widths $l_{1,2,3} = 7.5, 5.1, 3.7$ mT (based on spectral simulation). The resonance is observable at temperatures up to 50 K and corresponds to 90% of the Fe in the sample based on spin quantitations under nonsaturating conditions. A similar species was reported for cyanide-treated *D. desulfuricans* Dfx, $g_\perp = 2.27$ and $g_\parallel = 1.96$.[13]

(29) Jenney, F. E., Jr.; Adams, M. W. W. A., unpublished results.

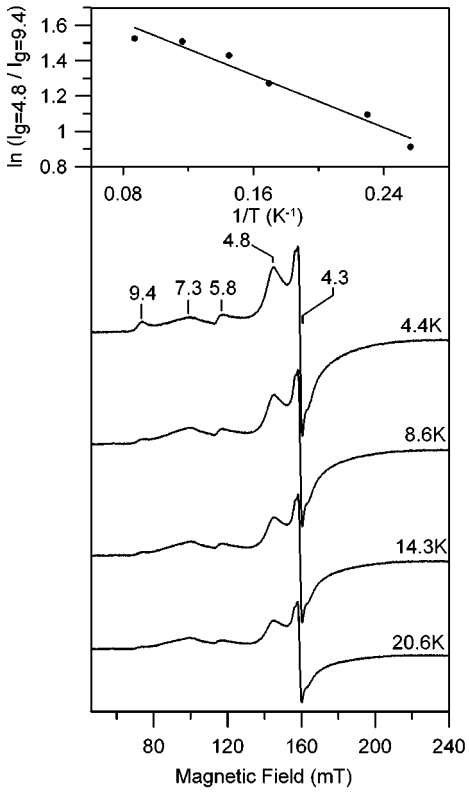

Figure 4. Temperature dependence of the EPR spectrum of recombinant *P. furiosus* SOR exchanged into 50 mM CHES buffer (pH 10.0). The sample and conditions of measurement are as described in Figure 1 except for the temperatures, which are indicated on the spectra. Selected *g*-values are shown on the 4.0 K spectrum. The inset shows a plot of $\ln(I_{g=4.8}/I_{g=9.4})$ versus $1/T$ which yields a straight line of slope -4.8 ± 0.4 K.

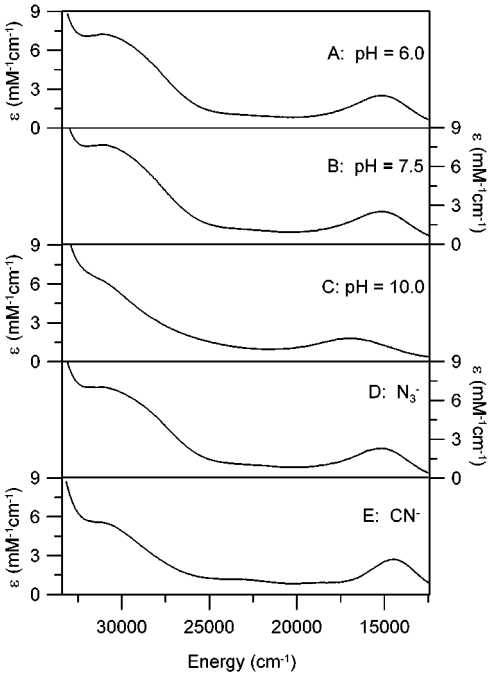

Figure 5. UV/visible absorption spectra of recombinant *P. furiosus* SOR: (A) 100 mM MES buffer (pH 6.0); (B) 50 mM HEPES buffer (pH 7.5); (C) 100 mM CHES buffer (pH 10.0); (D) sample B after addition of a 45-fold stoichiometric excess of sodium azide; (E) 50 mM TAPS buffer (pH 8.5), after addition of a 30-fold stoichiometric excess of sodium cyanide. All samples were ~0.3 mM in SOR and spectra were recorded in 1-mm cuvettes.

Absorption, CD, and VHVT MCD. (a) Oxidized *P. furiosus* SOR. The electronic excited-state properties of oxidized recombinant *P. furiosus* SOR were investigated using the combination of absorption, CD, and VHVT MCD. UV/visible absorption spectra recorded at pH 6.0, 7.5, and 10, and after addition of excess azide and cyanide, are shown in Figure 5. In each case the spectrum comprises an intense broad band centered near 30 000 cm^{-1} and a well-defined low-energy band centered between 14 000 and 17 500 cm^{-1}. The latter has been assigned to $(Cys)S^- \rightarrow Fe^{3+}$ charge transfer (CT) based on resonance Raman studies of the equivalent center in *D. desulfuricans* Dfx.[11] In accord with previous studies of *D. gigas* neelaredoxin,[6] the absorption spectrum *P. furiosus* SOR is pH dependent. The low-energy band centered at 15 150 cm^{-1} is invariant to pH over the range 6.0−8.5, but undergoes a blue shift to 17 000 cm^{-1} at pH 10.5 with a $pK_a = 9.6$ (see Supporting Information, Figure S2). Above pH 10.5, the site is readily and irreversibly lost, as evidenced by the progressive decrease in the absorption intensity at ~17 000 cm^{-1}. The addition of a 45-fold stoichiometric excess of sodium azide has no significant affect on the absorption spectrum. In contrast, cyanide binding, which induces a high-spin to low-spin transition as a result of increased d-orbital ligand-field splitting, is readily monitored by a red shift of the lower energy band to 14 600 cm^{-1}.

UV/visible CD and VHVT MCD studies were carried out on the samples of *P. furiosus* SOR used for absorption measurements. The absorption and EPR spectra were not perturbed by the addition of 55% (v/v) glycerol, which is required to form a low-temperature glass for VHVT MCD studies. Negligible, room-temperature CD was observed in the visible region for the high-spin Fe^{3+} forms, i.e., pH 7.5, pH 10, and N_3^- -bound (data not shown). However, VTMCD studies of the high-spin Fe^{3+} derivatives facilitate greater resolution of electronic transitions from the paramagnetic Fe chromophore and therefore more detailed assignments of ligand-to-metal CT bands (see Figure 6 and Table 1). Moreover, the analysis of VHVT MCD saturation magnetization data for transitions originating from the highly anisotropic ground-state Kramers doublets of a high-spin Fe^{3+} center provides polarization information that places additional constraints on electronic assignments (see Figure 7 and Table 1). Comparison of the spectra shown in Figures 5 and 6 demonstrates that the relative intensities of discrete transitions are quite different in the absorption and VTMCD spectra of the same sample. In this connection, it is important to emphasize that absorption intensity of symmetry-allowed ligand-to-metal CT bands is directly related to the extent of orbital overlap and thereby metal−ligand covalency. Hence, the symmetry-allowed $\sigma \rightarrow \sigma^*$, $(Cys)S(p) \rightarrow Fe^{3+}(d)$, and $\pi \rightarrow \pi^*$, $(Cys)S(p) \rightarrow Fe^{3+}(d)$ transitions associated with an Fe−S(Cys) unit would be expected to have intense $S \rightarrow Fe$ CT bands in the absorption spectrum. However, to a first approximation these are uniaxial transitions, polarized parallel to the Fe−S bond, and consequently are expected to exhibit weak VTMCD intensity. This is because the low-temperature MCD spectra of half-integer-spin transition metal centers are invariably dominated by *C*-terms that require *two* perpendicular, nonzero transition dipole moments for intensity.[30]

(30) Johnson, M. K. In *Physical Methods in Bioinorganic Chemistry. Spectroscopy and Magnetism*; Que, L., Jr., Ed.; University Science Books: Sausalito, CA, 2000; pp 233−286.

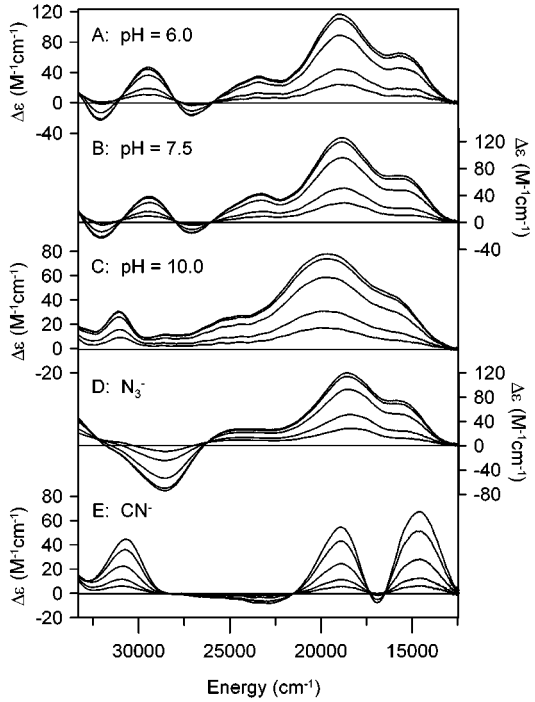

Figure 6. UV/visible VTMCD spectra of recombinant *P. furiosus* SOR. Samples are the same as those used in Figure 5 except for the addition of 55% (v/v) glycerol. Spectra were recorded with a magnetic field of 6 T at 1.68, 4.22, 10.0, 25.0, and 50.0 K. MCD intensity for all bands increases with decreasing temperature.

The VTMCD spectrum of *P. furiosus* SOR at pH 6.0 and 7.5 in the 13 000−22 000-cm^{-1} region is dominated by two positive *C*-terms centered at 15 150 and 18 980 cm^{-1} (see Figure 6), with the former corresponding to the intense absorption band centered at 15 150 cm^{-1}. These bands are in the region expected for S → Fe^{3+} CT transitions involving the filled S p-orbitals and the half-filled t_{2g} set of Fe d-orbitals ($d_{xy,yz,xz}$) that are available for π bonding, and the lower energy transition is assigned to the $\pi \rightarrow \pi^*$ transition with optimal π interaction. By analogy with the detailed assignments that are available for blue copper proteins,[31] the three S p-orbitals of the cysteinate are expected to split with one being primarily σ bonding to carbon and therefore not significantly involved in bonding to the metal. The other two S p-orbitals are perpendicular to the S−C bond and will be degenerate for free cysteinate. For an Fe-ligated cysteine, these two S p-orbitals will split into a higher energy p_π-orbital that is perpendicular to the Fe−S−C plane and available for direct π overlap with the Fe t_{2g} d-orbital that is perpendicular to the Fe−S−C plane and a lower energy $p_{pseudo\ \sigma}$-orbital that is in the Fe−S−C plane with the extent of σ interaction being determined by the Fe−S−C angle (maximal for a 90° angle) (see Figure 8). Since the average of the Fe−S−C angles in the crystal structure of oxidized *P. furiosus* SOR is close to 120°,[8] the $p_{pseudo\ \sigma}$-orbital will have σ overlap with the Fe d-orbital oriented along the Fe−S bond and π overlap with the Fe t_{2g} d-orbital that lies within the Fe−S−C plane.

VHVT MCD saturation magnetization studies were carried out for the MCD bands centered at 15 150 and 18 980 cm^{-1} (see Figure 7) to assess the transition polarizations with respect to the unique (*z*) axis of the predominantly axial zero-field splitting ($E/D = 0.06$). Because the axial zero-field splitting of the $S = {}^5/_2$ ground state, $D = -0.50$ cm^{-1}, is comparable to the Zeeman interaction at fields up to 6 T, it is not appropriate to analyze only the lowest temperature data (isotherm at 1.7 K) under the assumption that the magnetization data are determined solely by the effective *g*-values of the lowest doublet.[30] Rather, as the Zeeman splitting increases, the electron spin changes from being quantized along the molecular zero-field splitting axis to being quantized along the applied field direction. Neese and Solomon developed a comprehensive methodology for analyzing VHVT MCD magnetization data in this regime.[26] Since the zero-field splitting parameters are determined by EPR ($D = -0.50$ cm^{-1}, $E/D = 0.06$), the only variable parameters involved in the fitting procedure are a scaling factor and the effective *xy*, *yz*, and *xz* transition dipole moments, M_{xy}, M_{yz}, and M_{xz}, respectively, which approximate to the product of the two linear transition dipole moments.[32] The MCD magnetization data collected at 15 150 cm^{-1} (corresponding to the absorption maximum) and at 18 980 cm^{-1} are quite different (see Figure 7), and the differences can be rationalized exclusively in terms of transition polarization. The VTMCD intensity at the 15 150-cm^{-1} band originates from a predominantly *y*-polarized transition, whereas the 18 980-cm^{-1} band is predominantly *z* polarized. Since the 15 150-cm^{-1} band corresponds to the $\pi \rightarrow \pi^*$ (Cys)S(p) → Fe^{3+}(d) transition, the MCD magnetization data indicate that the Fe−S bond is along the *y*-axis with respect to the zero-field splitting axis system.

The visible region (Cys)S^- → Fe^{3+} CT transitions that are observed in the absorption and VTMCD spectra for *P. furiosus* SOR at pH 6.0 and 7.5 can now be assigned on the basis of the EPR-determined ground-state properties and transition polarizations deduced from MCD magnetization measurements. An axial ground state ($E/D = 0.06$) with negative axial zero-field splitting ($D = -0.5$ cm^{-1}) is consistent with tetragonally compressed octahedral coordination, i.e., octahedral with a strong ligand field along the *z*-axis.[33] Since the Fe−S bond is along the *y*-axis, the *z*-axis must correspond to one of the two pairs of trans (His)N ligands. Hence, the half-filled t_{2g} set of Fe d-orbitals will split, with a near-degenerate pair, d_{xz} and d_{yz}, higher in energy than d_{xy} (see Figure 8). For the molecular *z*-axis parallel to the Fe−S−C plane, an appropriate orbital energy level diagram for the S 3p- and Fe 3d-orbitals is shown in Figure 8. Two (Cys)S^- → Fe^{3+} CT transitions are predicted in the visible region. The lower energy transition is the *y*-polarized S(p_π) → Fe(d_{xy}) transition that is predicted to be strong in absorption due to optimal π interaction, but weak in the VTMCD spectrum, since it is a uniaxial transition polarized almost exclusively along the Fe−S bond. Hence the S(p_π) → Fe(d_{xy}) transition is assigned to the absorption and VTMCD bands centered at 15 150 cm^{-1} (see Table 1). The higher energy transition is the predominantly *z*-polarized S($p_{pseudo\ \sigma}$) → Fe(d_{yz}) transition that is expected to be weak in absorption due to weak π overlap, but strong in the VTMCD spectrum due to equal and opposite mixing of *x*- and *y*-polarized components. Hence, the S($p_{pseudo\ \sigma}$) → Fe(d_{yz})

(31) (a) Gewirth, A. A.; Solomon, E. I. *J. Am. Chem. Soc.* **1988**, *110*, 3811−3819. (b) LaCroix, L. B.; Randall, D. W.; Nersissian, A. M.; Hoitink, C. W. G.; Canters, G. W.; Valentine, J. S.; Solomon, E. I. *J. Am. Chem. Soc.* **1998**, *120*, 9621−9631.

(32) Uniaxial polarization percentages have been estimated from M_{xy}, M_{yz}, and M_{xz}, using the cyclic permutations of the following expression:[26] $\% x = 100(M_{xy}M_{xz})^2/[(M_{xy}M_{xz})^2 + (M_{xy}M_{yz})^2 + (M_{xz}M_{yz})^2]$.

(33) Solomon, E. I.; Brunold, T. C.; Davis, M. I.; Kemsley, J. N.; Lee, S.-K.; Lehnert, N.; Neese, F.; Skulan, A. J.; Yang, Y.-S.; Zhou, J. *Chem. Rev.* **2000**, *100*, 235−349.

Table 1. Excited-State Electronic Assignments for Derivatives of Oxidized Recombinant *P. furiosus* SOR[a]

	absorption			MCD			CD	
assignments	energy, cm^{-1} (nm)	ϵ, $mM^{-1}\,cm^{-1}$	predicted polarization	energy, cm^{-1} (nm)	sign	observed polarization	energy, cm^{-1} (nm)	sign
oxidized SOR pH 7.5								
$CysS^- \rightarrow Fe^{3+}$ CT								
$S(p_\pi) \rightarrow Fe(d_{xy})$	15 150 (660)	2.5	*y*	15 150 (660)	+	*y*		
$S(p_{pseudo\ \sigma}) \rightarrow Fe(d_{yz})$			*z*	18 980 (527)	+	*z*		
				23 430 (427)	+	*z*		
				27 040 (370)?	−			
His $\rightarrow Fe^{3+}$ CT	~30 000 (333)	7.2	*x* or *z*	29 480 (339)	+	*z*		
				32 130 (311)?	−			
oxidized SOR pH 10.0								
$CysS^- \rightarrow Fe^{3+}$ CT								
$S(p_\pi) \rightarrow Fe(d_{xy})$	16 940 (590)	1.8	*y*	16 500 (606)	+	*y*		
$S(p_{pseudo\ \sigma}) \rightarrow Fe(d_{yz})$			*z*	19 720 (507)	+	*z*		
				24 200 (405)	+	*z*		
His $\rightarrow Fe^{3+}$ CT	~31 000 (333)	6.2	*x* or *z*	31 060 (322)	+	*z*		
oxidized SOR + N_3^-								
$CysS^- \rightarrow Fe^{3+}$ CT								
$S(p_\pi) \rightarrow Fe(d_{xy})$	15 150 (660)	2.3	*y*	15 150 (660)	+	*y*		
$S(p_{pseudo\ \sigma}) \rightarrow Fe(d_{yz})$			*z*	18 980 (527)	+	*z*		
				23 430 (427)	+	*z*		
His $\rightarrow Fe^{3+}$ CT	~30 000 (333)	6.5	*x* or *z*	33 700 (296)?	+			
$N_3^- \rightarrow Fe^{3+}$ CT				28 520 (351)	−	*y*		
oxidized SOR + CN^-								
$CysS^- \rightarrow Fe^{3+}$ CT								
$S(p_\pi) \rightarrow Fe(d_{yz})$	14 600 (685)	2.7	*y*	14 680 (681)	+			
				17 000 (588)	−			
				19 000 (526)	+			
							20 610 (485)	+
low-spin Fe^{3+} d−d				23 000 (435)	−		22 710 (440)	+
							26 650 (375)	−
							30 120 (332)?	−
							32 620 (307)?	−
His $\rightarrow Fe^{3+}$ CT	~31 000 (322)	5.8	*x* or *z*	30 800 (325)?	+			
$CN^- \rightarrow Fe^{3+}$ CT			*y*	30 800 (325)?	+			

[a] Assignments marked with a question mark are tentative, since polarization data are not currently available; see Figure 8 for the axis systems used in the assignments of the high-spin (pH 7.5, pH 10, N_3^-) and low-spin (CN^-) forms of oxidized SOR.

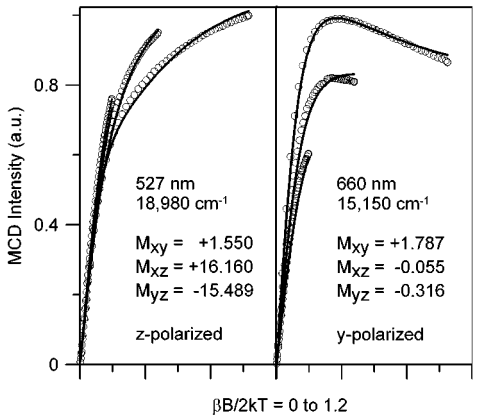

Figure 7. VHVT MCD saturation magnetization data for recombinant *P. furiosus* SOR at pH 7.5. The sample corresponds to Figure 6B, and the data were collected at fixed temperatures of 1.68, 4.22, and 10.0 K for magnetic fields in the range 0−6 T. The solid lines are best fits using the EPR-determined zero-field splitting parameters with M_{xy}, M_{xz}, and M_{yz} as variable parameters. Uniaxial polarizations are estimated to be 98% *z*, 1% *x*, and 1% *y* at 23 430 and 18 980 cm^{-1} and 98% *y* and 2% *x* at 15 151 cm^{-1}.[32]

transition is assigned to the VTMCD band centered at 18 980 cm^{-1} that is not resolved in the absorption spectrum (see Table 1).

The VTMCD spectra of *P. furiosus* SOR at pH 6.0 and 7.5 resolve four transitions in the 22 000−33 000-cm^{-1} region under the broad envelop of the absorption band centered at ~30 000 cm^{-1}, positive MCD bands centered at 23 430 and 29 480 cm^{-1}, and two negative bands centered at 27 040 and 32 130 cm^{-1}. On the basis of the active-site structure, several LMCT transitions are expected in this region: *x*- or *z*-polarized π His $\rightarrow Fe^{3+}$ CT bands involving the three Nϵ and one Nδ equatorial His ligands, a *y*-polarized $\sigma \rightarrow \sigma^*$, $S(p_{pseudo\ \sigma}) \rightarrow Fe^{3+}(d_{x^2-y^2})$ CT band, and a *y*-polarized glutamate-to-Fe^{3+} CT band. VHVT MCD saturation magnetization data collected at 23 430 and 29 480 cm^{-1} (data not shown) are very similar to that obtained at 18 980 cm^{-1} (see Figure 7) and are readily analyzed in terms of predominantly *z*-polarized transitions. This demonstrates that π His $\rightarrow Fe^{3+}$ CT transitions contribute to the broad absorption band at 30 000 cm^{-1} but does not rule out contributions from $\sigma \rightarrow \sigma^*$, $S(p_{pseudo\ \sigma}) \rightarrow Fe^{3+}(d_{x^2-y^2})$ CT or glutamate-to-Fe^{3+} CT transitions. Additional VHVT MCD saturation studies, coupled with resonance Raman excitation profiles, electronic structure calculations, and mutagenesis studies, will be required to effect detailed electronic assignments in this region.

The above assignments are readily transferred to the other two high-spin *P. furiosus* SOR derivatives investigated in this work (see Table 1). The high-pH form exhibits the same pattern of S $\rightarrow$ Fe CT bands in the visible VTMCD spectrum with equivalent transitions blue shifted by ~750 cm^{-1}. The VTMCD spectrum is broader and less well resolved than that of the low-pH form, due to contributions from the low-pH form at pH 10

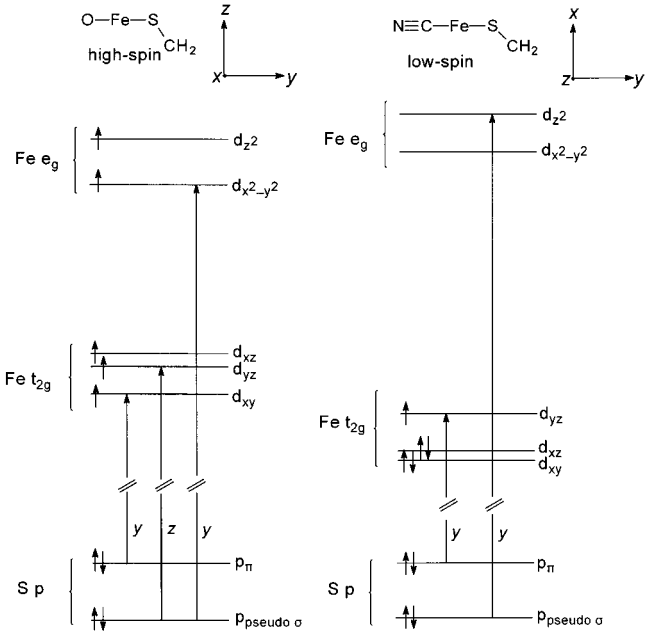

Figure 8. Schematic orbital energy level diagram and depiction of the (Cys)S(p) → Fe^{3+}(d) charge-transfer transitions associated with the as-prepared (high-spin) and CN^--bound (low-spin) octahedral Fe^{3+} centers in SOR. Uniaxial polarizations corresponding to the axis systems shown are indicated to the right of each transition. The relative orbital energies are based on the electronic assignments and the EPR properties, as discussed in the text.

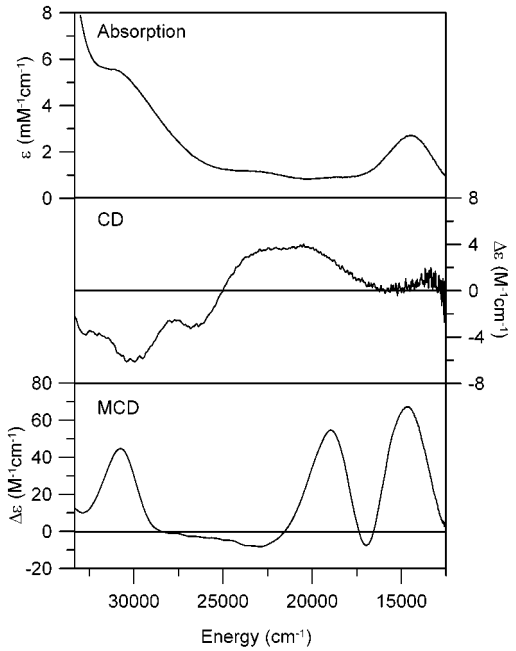

Figure 9. Comparison of the UV/visible absorption, CD, and VTMCD spectra of cyanide-bound recombinant *P. furiosus* SOR. The sample is the same as that described in Figure 5E, except for the addition of 55% (v/v) glycerol for the samples used for CD and VTMCD. The absorption spectrum was recorded at room temperature. The MCD spectrum was recorded at 1.68 K and 6 T, and the CD spectrum was recorded at 4.22 K. None of the observed CD bands results from strain in the frozen glass, since an equivalent, albeit less well-resolved, spectrum was observed at room temperature.

(pK_a = 9.6). This heterogeneity complicates the higher energy CT region of the MCD spectrum (22 000−33 000 cm^{-1}), but high-pH minus low-pH difference spectra reveal the same pattern of VTMCD bands with equivalent bands blue shifted by ∼1500 cm^{-1}. This indicates that the cysteinyl and histidyl Fe ligation are preserved in the high-pH form and suggests that high-pH transition involves hydroxyl ligation trans to cysteine. Azide binding does not perturb the VTMCD bands in the S → Fe CT region but is evident by the appearance of an intense negative band centered at 28 520 cm^{-1} that dominates the higher energy CT region. This band is attributed to N_3^- → Fe^{3+} CT on the basis of VHVT MCD saturation magnetization data (not shown). The magnetization data are analogous to that observed at 15 150 cm^{-1} in Figure 7, indicating a *y*-polarized transition, which is consistent with N_3^- binding trans to the cysteinyl S.

Cyanide binding induces a high-spin to low-spin transition and is manifest by small changes in the absorption spectrum (Figure 5), marked changes in the VTMCD spectrum (Figure 6), and the appearance of pronounced CD bands above 17 000 cm^{-1} (Figure 9). VHVT MCD saturation data for each of the major bands in the VTMCD spectrum are well fit at all temperatures by simulated data constructed for an isolated $S = {}^1/_2$ doublet using the EPR determined *g*-values, g = 2.289, 2.251, 1.935 (data not shown). The range of *g*-values is not sufficient to permit meaningful assessment of transition polarizations by fitting of the saturation magnetization data. However, analysis of the visible S → Fe^{3+} CT bands for a low-spin system is greatly simplified, since there is only one hole in the t_{2g} set of Fe d-orbitals. Moreover, the splitting of the t_{2g} set of d-orbitals can be assessed from the EPR spectrum using the relationships between principal *g*-values, *V*, Δ, and ξ developed by Taylor[34]

(where *V* and Δ and the rhombic and axial splitting parameters for the t_{2g} set of d-orbitals and ξ is the one-electron spin−orbit coupling constant for Fe):

$$V/\xi = g_x/(g_x + g_y) + g_y/(g_z - g_x)$$

$$\Delta/\xi = g_x/(g_z + g_y) + g_z/(g_y - g_x) - V/2\xi \qquad (2)$$

Using the EPR-determined *g*-values for CN^--bound *P. furiosus* SOR, with g_z, g_y, and g_x as the highest, middle and lowest *g*-values, respectively, eq 2 yields V/ξ = 6.82, Δ/ξ = 4.26, and V/Δ = 1.60. A reasonable estimate of ξ for Fe in a complex with significant covalent bonding is ∼ 400 cm^{-1}, which leads to V ∼ 2700 cm^{-1} and Δ ∼ 1700 cm^{-1}, and the t_{2g} orbital splitting pattern shown in Figure 8 with d_{yz} and d_{xz} separated by ∼2700 cm^{-1} and d_{xz} and d_{xy} near degenerate and separated by ∼350 cm^{-1}. Hence, the EPR indicates tetragonally elongated octahedral coordination geometry with the weak-field axis along *x*, as dictated by the axis system adopted for the *g*-tensor. The implication is that binding cyanide trans to the cysteinate results in a strong-field axis comparable to the strong-field bis-histidyl axis that is responsible for the tetragonal compression of the high-spin derivatives discussed above. A d-orbital splitting diagram for the *x*-axis along the weak-field bis-histidyl axis and the Fe−S bond along the *y*-axis is shown in Figure 8.

Only one (Cys)S^- → Fe^{3+} CT transition is predicted to occur in the visible region, corresponding to the *y*-polarized, S(p_π) → Fe(d_{yz}) $\pi \rightarrow \pi^*$ transition (see Figure 8). This transition is expected to have strong absorption intensity as a result of optimal orbital overlap and weak VTMCD intensity since it is primarily a uniaxial transition. Some VTMCD intensity is

(34) Taylor, C. P. S. *Biochim. Biophys. Acta* **1977**, *491*, 137−149.

expected since the hole in the t_{2g} set of Fe d-orbitals is best considered as a linear combination of all three one-electron d-orbitals, with coefficients that are defined by the EPR *g*-values.[34,35] Hence, the intense absorption band centered at 14 600 cm^{-1} and the positive VTMCD band centered at 14 680 cm^{-1} are assigned to the $S(p_\pi) \rightarrow Fe(d_{yz})$ $\pi \rightarrow \pi^*$ transition (see Table 1).

In the low-spin cyanide adduct, multiple spin-allowed Fe d−d bands are expected with energies of >17 000 cm^{-1}. Such bands are expected to be weak and difficult to see in absorption, particularly in the presence of intense LMCT bands. However, since they are magnetic dipole-allowed transitions, they are expected to be more clearly apparent in the CD and VTMCD spectra. Indeed, cyanide addition results in the appearance of broad positive CD bands centered at 20 610 and 22 710 cm^{-1} and broad negative CD bands centered at 26 650, 30 120, and 32 620 cm^{-1}. These CD bands appear to correlate with positive VTMCD bands centered at 19 000 and 31 000 cm^{-1} and negative VTMCD bands centered at 17 000 cm^{-1} and in the 22 000−27 000-cm^{-1} region (see Figure 9). These bands are all excellent candidates for the complex pattern of ligand field $^2T_2 \rightarrow {}^2A_2$, $^2T_1$, $^2T_2$, ^2E, $^2T_1$, $^2A_2$, $^2T_2$ transitions (under idealized O_h symmetry) that are expected with increasing energy in the 17 000−35 000-cm^{-1} region. On the basis of the lowest energy ligand-field transitions, the ligand-field parameters are estimated to be $10Dq \sim 22\,000$ cm^{-1} and $B \sim 750$ cm^{-1}. Analysis of the high-energy region of the UV/visible absorption, CD and VTMCD spectra (22 000−35 000 cm^{-1}) is a complex problem due to overlapping contributions for ligand field, π His $\rightarrow Fe^{3+}$ CT and $CN^- \rightarrow Fe^{3+}$ CT transitions. More detailed ligand-field analyses and DFT calculations are in progress to effect assignments of the ligand-field and CT transitions and more accurate assessment of the ligand-field parameters.

(b) Reduced *P. furiosus* SOR. Reduction of *P. furiosus* SOR with ascorbate or dithionite occurs with complete bleaching of the blue color and results in samples with no absorption in the visible region. However, the combination of absorption, CD, and VTMCD studies in the UV and near-IR regions facilitates investigation of CT and ligand-field transitions, and the results provide unique insight into the structural, electronic, and magnetic properties of the high-spin ($S = 2$) Fe^{2+} active site. The UV absorption is dominated by the intense absorption centered at 36 000 cm^{-1} that arises from aromatic amino acid residues, and the only feature attributable to CT transitions associated with the Fe^{2+} active site is the shoulder at 31 200 cm^{-1} (see Figure 10). In contrast, VTMCD provides a means of selectively investigating the electronic transitions associated with the paramagnetic Fe^{2+} active site. The positively signed temperature-dependent MCD band at 31 200 cm^{-1} correlates with the observable absorption band, and additional CT transitions are identified by a positive MCD bands centered at 33 900 and 38 900 cm^{-1} (see Figure 10). The correspondence to the visible VTMCD bands assigned to $(Cys)S^- \rightarrow Fe^{3+}$ CT transitions in oxidized high-spin derivatives of *P. furiosus* SOR (see Table 1 and Figure 6) is particularly striking. The signs and relative intensity of individual transitions are the same, and the only difference is that the corresponding transitions are shifted to higher energy by ∼15 500 cm^{-1} in reduced SOR.

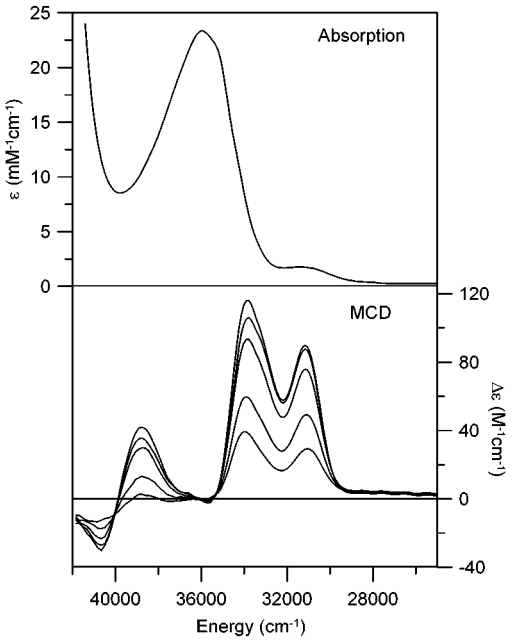

Figure 10. UV absorption and VTMCD spectra of ascorbate-reduced recombinant *P. furiosus* SOR. The sample was 0.9 mM in SOR and was in 100 mM D_2O MOPS buffer (pD 7.5), with 55% (v/v) glycerol-d_3. Upper panel: room-temperature absorption spectrum in a 1-mm path length cell. Lower panel: VTMCD spectra recorded in a 1-mm path length cell at 1.70, 4.22, 10.2, 24.3, and 52.0 K with an applied field of 6 T. All MCD bands increase in intensity with decreasing temperature.

Hence, the positively signed VTMCD bands at 31 200 and 33 900 cm^{-1} are tentatively assigned to an analogous set of $(Cys)S^- \rightarrow Fe^{2+}$ CT transitions. More detailed assignments are presented below, following assessment of the Fe d-orbital splittings via analysis of the ligand-field transitions.

The seminal work of Solomon and co-workers on reduced mononuclear Fe proteins and model complexes has laid a firm foundation for interpreting the ligand-field transitions that are observable in near-IR absorption, CD, and VTMCD spectra, in terms of coordination geometry and d-orbital splitting.[27,33] Near-IR absorption, CD, and VTMCD spectra for ascorbate-reduced *P. furiosus* SOR in D_2O buffer are shown in Figure 11, and corresponding VTMCD spectra after the addition of a 45-fold excess of azide and a 30-fold excess of cyanide are shown in Figures12 and 13, respectively. Absorption spectra are of limited utility in this region, since O−H stretching overtones from unexchanged water and protein groups and O−D stretching overtones obscure the region below 9000 cm^{-1}. CD spectra are not reliable below 6000 cm^{-1} due to the intense O−D overtone absorption and the possibility of contributions from protein vibrational CD. VTMCD spectra provide the most definitive assessment of ligand field transitions in the 14 000−5000-cm^{-1} region, since temperature-dependent bands must originate from a paramagnetic Fe^{2+} center.

The near-IR absorption spectrum of reduced *P. furiosus* SOR has a weak, broad band centered at 12 100 cm^{-1}, with corresponding positive CD band centered at 12 200 cm^{-1} and negative, temperature-dependent MCD band centered at 12 400 cm^{-1} (see Figure 11). Although it is not possible to record VTMCD spectra at energies below 5000 cm^{-1} with the currently available instrumentation, the high-frequency tail of a positive, temperature-dependent MCD band centered at <5000 cm^{-1} is readily apparent. The observation of two ligand-field transitions,

(35) McKnight, J.; Cheesman, M. R.; Thomson, A. J.; Miles, J. S.; Munro, A. W. *Eur. J. Biochem.* **1993**, 683−687.

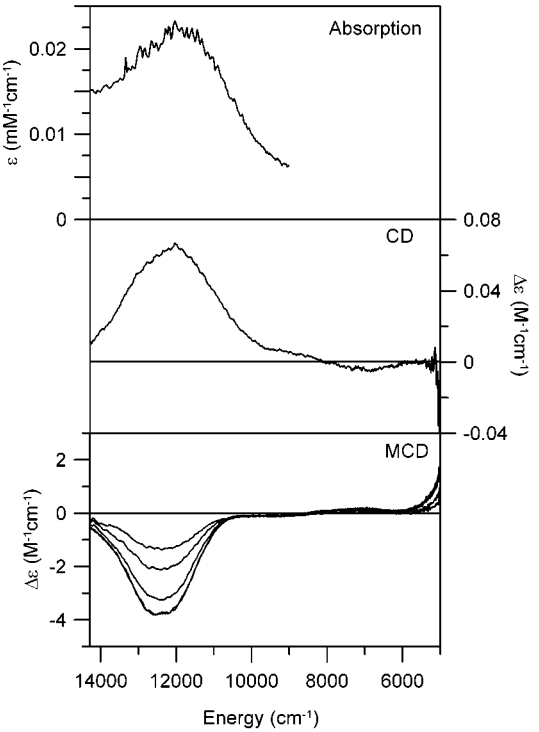

Figure 11. Near-IR absorption, CD and VTMCD spectra of ascorbate-reduced recombinant *P. furiosus* SOR. The sample was 4.5 mM in SOR and was in 100 mM D_2O MOPS buffer (pD 7.5), with 55% (v/v) glycerol-d_3. Upper panel: room-temperature absorption spectrum. Middle panel: room-temperature CD spectrum. Lower panel: VTMCD spectra. All MCD bands increase in intensity with decreasing temperature.

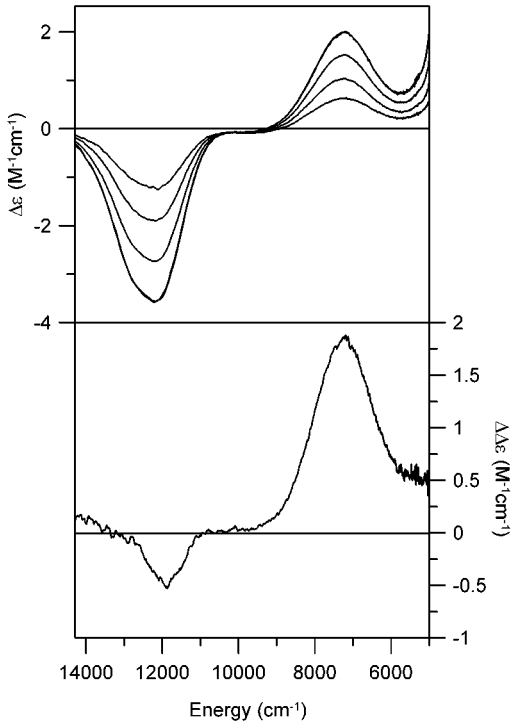

Figure 12. Near-IR VTMCD spectra of ascorbate-reduced recombinant *P. furiosus* SOR in the presence of a 45-fold stoichiometric excess of azide. The sample is as described in Figure 11 except for the addition of a 45-fold stoichiometric excess of sodium azide. Upper panel: VTMCD spectra recorded in a 1-mm path length cell at 1.70, 4.22, 10.2, 24.6, and 51.0 K with an applied field of 6 T. All MCD bands increase in intensity with decreasing temperature. Lower panel: MCD difference spectrum corresponding to the azide-treated ascorbate-reduced spectrum at 1.70 K minus 85% of the ascorbate-reduced spectrum recorded under the same conditions.

one $>10\,000$ cm^{-1} and one $\sim$5000 cm^{-1}, is characteristic of a five-coordinate, square-pyramidal Fe^{2+} site.[27,33] This is readily understood in terms of a large splitting in the ^5E_g excited state of the parent $^5T_{2g} \rightarrow {}^5E_g$ octahedral d−d band (Δ^5E_g), as a result of removal of one ligand along the *z* axis, i.e., large splitting of the $d_{x^2-y^2}$ and d_{z^2} orbitals (see Figure 14). Hence, the VTMCD data indicate square-pyramidal coordination geometry with $10Dq < 8700$ cm^{-1} and $\Delta^5E_g > 7400$ cm^{-1} (see Table 2).

Definitive evidence for azide and cyanide binding at the vacant coordination site of the square-pyramidal Fe^{2+} site is provided by near-IR VTMCD studies. The addition of a 45-fold excess of azide did not significantly perturb the NIR absorption and CD spectra, but results in the appearance of positive VTMCD band centered at 7300 cm^{-1} and weak negative band at 12 100 cm^{-1} (Figure 12). The latter band is superimposed on the intense negative VTMCD band centered at the 12 400-cm^{-1} band from the square-pyramidal reduced form (Figure 11). The VTMCD bands associated with the reduced azide-bound form are readily apparent after subtraction of 85% of the reduced SOR VTMCD spectrum (Figure 12). Hence, only 15% of the reduced SOR has azide-bound in samples treated with a 45-fold stoichiometric excess of azide, and the weak binding presumably accounts for the absence of significant changes in the NIR absorption and CD spectra. The addition of a 30-fold excess of cyanide is marked by a shift in the near-IR absorption from 12 100 cm^{-1} to a broad band centered at 11 500 cm^{-1} (not shown). Both the CD and VTMCD spectra facilitate resolution of this band into two transitions: positive and negative CD bands centered at 9900 and 11 600 cm^{-1}, respectively, and positive and negative VTMCD bands centered at 10 100 and 11 900 cm^{-1}, respectively (Figure 13). Once again the VTMCD data show evidence for the presence of some of the unbound, square-pyramidal form. Subtraction of 20% of the reduced SOR spectrum is required to obtain the VTMCD characteristics of the cyanide-bound Fe^{2+} species in isolation (Figure 13). Hence, $\sim$80% of the reduced SOR has cyanide bound in samples treated with a 30-fold stoichiometric excess of cyanide.

The ligand-field transitions for cyanide-bound reduced SOR, i.e., two components of $^5T_{2g} \rightarrow {}^5E_g$ at 10 000 and 11 800 cm^{-1}, corresponding to $10Dq = 10\,900$ cm^{-1} and $\Delta^5E_g = 1800$ cm^{-1} (Table 2), are characteristic of a six-coordinate octahedral Fe^{2+} site.[27,33] However, the ligand-field transitions for azide-bound reduced SOR, i.e., two components of $^5T_{2g} \rightarrow {}^5E_g$ at 7300 and 12 100 cm^{-1}, corresponding to $10Dq = 9700$ cm^{-1} and $\Delta^5E_g = 4800$ cm^{-1} (Table 2), indicate a coordination geometry intermediate between square pyramidal and octahedral. The implication is that azide is only weakly bound at the vacant coordination site. With respect to the d-orbital energy diagram shown in Figure 14, the major consequence of azide or cyanide binding at the vacant coordination site is to increase the energy of the d_{z^2} orbital. The small changes in the energy of the $d_{x^2-y^2}$ orbital as a function of exogenous ligand binding suggest that movement of the Fe into the equatorial plane is compensated by weaker Fe−N bonding in the six-coordinate species.

Analysis of VHVT MCD saturation magnetization data using the protocols developed by Solomon and co-workers for mononuclear $S = 2$ Fe^{2+} sites[27,33] provides information on

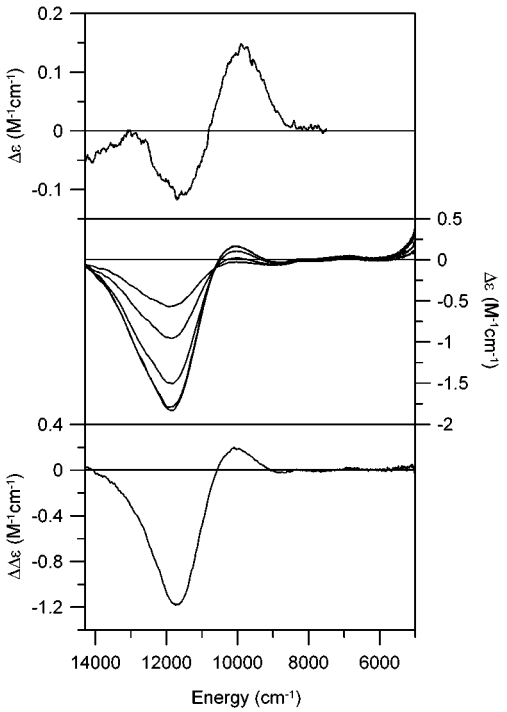

Figure 13. Near-IR CD and VTMCD spectra of ascorbate-reduced recombinant *P. furiosus* SOR in the presence of a 30-fold stoichiometric excess of cyanide. The sample is as described in Figure 11 except for the addition of a 30-fold stoichiometric excess of potassium cyanide. Upper panel: CD spectrum recorded at 4.22 K. Middle panel: VTMCD spectra recorded in a 1-mm path length cell at 1.70, 4.22, 10.0, 25.2, and 52.0 K with an applied field of 6 T. All MCD bands increase in intensity with decreasing temperature. Lower panel: MCD difference spectrum corresponding to the cyanide-treated ascorbate-reduced spectrum at 1.70 K minus 20% of the ascorbate-reduced spectrum recorded under the same conditions.

Table 2. NIR Excited-State Transition Energies and Ligand-Field Splittings for High-Spin Fe^{2+} Center in Reduced Recombinant *P. furiosus* SOR

sample	method[a]	observed d–d transitions,[b] cm^{-1}		$10Dq$, cm^{-1}	Δ^5E_g, cm^{-1}
as-prepared	Abs	12100			
	CD	12200 (+)			
	MCD	12400 (−)	<5000 (+)	<8700	>7400
azide-bound[c]	MCD	12100 (−)	7300 (+)	9700	4800
cyanide-bound[c]	Abs	11500			
	CD	11600 (−)	9900 (+)	10800	1700
	MCD	11900 (−)	10100 (+)	11000	1800

[a] Absorption at room temperature, CD at room temperature and 1.6 K, and MCD at 1.6 K. [b] Signs of CD and MCD bands are given in parentheses. [c] The azide- and cyanide-bound forms are both mixtures of exogenous ligand-bound forms and as-prepared square-pyramidal forms. The parameters shown are only for the ligand-bound forms.

ground-state zero-field splitting and thereby the splitting of the t_{2g} (d_{xy}, d_{xz}, d_{yz}) set of orbitals. MCD saturation magnetization data for reduced SOR collected at 12 400 cm^{-1} are shown in Figure 15. The high degree of nesting for data collected at 1.70, 4.22, and 10.4 K is characteristic of a ground state with $-D$ and large rhombic splitting, δ, in the lowest lying "$M_s = \pm 2$ doublet" or a ground state with $+D$, which leaves the $M_s = 0$ singlet lowest in energy. However, attempts to fit the data to the $-D$ model, and allowing for a substantial B-term component (up to 4% of C-term), gave values of $\delta = 7 \pm 1$ cm^{-1} and $g_{||} = 9 \pm 2$, which corresponds to spin Hamiltonian parameters of $D = -21 \pm 3$ cm^{-1} and $E/D = 0.33$. Such a large value of D

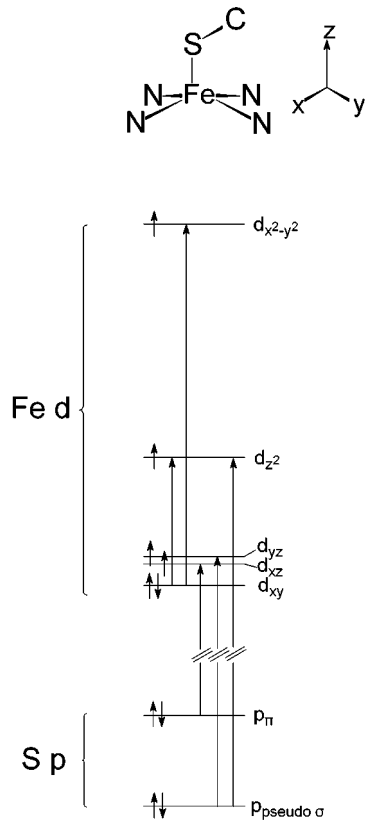

Figure 14. Schematic orbital energy level diagram for the square-pyramidal Fe^{2+} center in reduced SOR and depiction of the Fe d−d and proposed $(Cys)S^- \rightarrow Fe^{2+}$ CT transitions. The relative orbital energies are based on the electronic assignments and VTVH MCD saturation data discussed in the text.

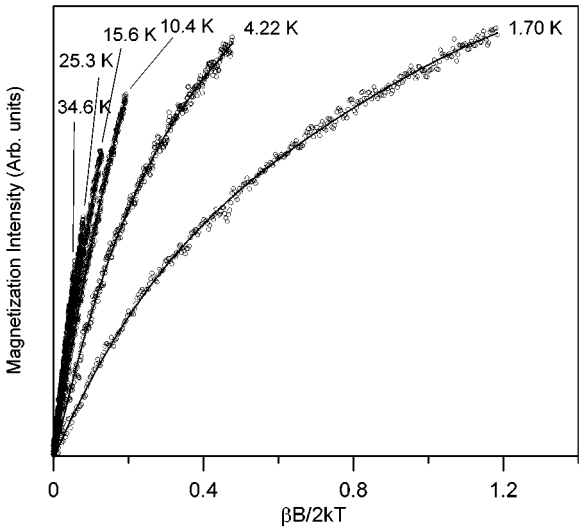

Figure 15. VHVT MCD saturation magnetization data for ascorbate-reduced recombinant *P. furiosus* SOR collected at 12 400 cm^{-1}. Data collected at 1.70, 4.22, 10.4, 15.6, 25.3, and 34.6 K with magnetic fields between 0 and 6 T. Solid lines are theoretical data computed according to ref 27 for an *xy*-polarized transition from a three-level $+D$ model with a zero-field energy level spacing of 0, 7, and 15 cm^{-1} between the lowest three components of the $S = 2$ ground state.

is unprecedented for high-spin Fe^{2+} species[27] and suggests that a $+D$ fit is more appropriate. The data are readily fit with a three-level $+D$ model (i.e., ignoring contributions from higher lying $M_s = \pm 2$ levels), with an energy level spacing of 0, 7,

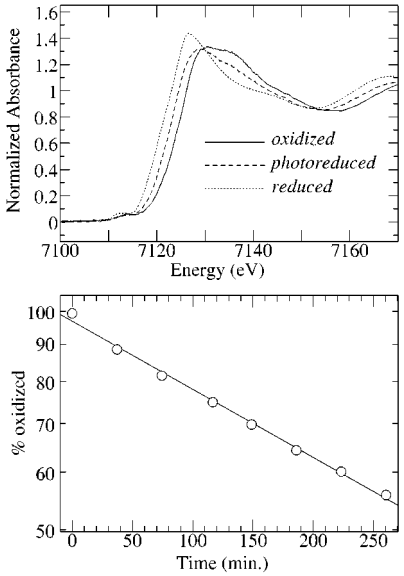

Figure 16. Upper panel: Iron K near-edge spectra of recombinant *P. furiosus* SOR in air-oxidized, dithionite-reduced, and 4.5-h photoreduced forms. The samples of SOR (4 mM) were in 50 mM Tris-HCl buffer (pH 7.8) with 55% (v/v) glycerol and were reduced with a 5-fold excess of sodium dithionite. Lower panel: Kinetics of X-ray-induced photoreduction estimated by curve fitting of individual scans to linear combination of oxidized (5-min beam exposure) and dithionite-reduced spectra. The ordinate scale is logarithmic. The beam current varied from 80 to 82 mA during the experiment.

and 15 cm^{-1}, corresponding to $D \sim +10$ cm^{-1} and $E/D \sim 0.1$. This translates to ligand-field parameters $\Delta = +700 \pm 200$ cm^{-1} and $|V/2\Delta| = 0.19 \pm 0.05$ and the splitting pattern shown in Figure 14 with d_{xz} and d_{yz} split by ~170 cm^{-1} and d_{xy} ~ 700 cm^{-1} lower in energy than the average of d_{xz} and d_{yz}.

The d-orbital splitting deduced from ligand-field spectroscopy suggests plausible assignments the UV VTMCD bands as $(Cys)S^- \rightarrow Fe^{2+}$ CT transitions (see Figure 14). The positively signed bands at 31 200 and 33 900 cm^{-1} (Figure 10) are assigned to *z*-polarized $S(p_\pi) \rightarrow Fe^{3+}(d_{xz})$ and the *y*-polarized, $S(p_{pseudo\ \sigma}) \rightarrow Fe(d_{yz})$ $\pi \rightarrow \pi^*$ transition, respectively. The $S(p_\pi) \rightarrow Fe^{3+}(d_{xz})$ $\pi \rightarrow \pi^*$ transition is expected to be strong in absorption due to optimal overlap and weak in the VTMCD spectrum since it is a uniaxial transition. In contrast, the $S(p_{pseudo\ \sigma}) \rightarrow Fe(d_{yz})$ $\pi \rightarrow \pi^*$ transition is expected to be weak in absorption due to poor overlap but strong in the VTMCD spectrum due to significant mixing with orthogonally polarized components. Since the d_{z^2} orbital is ~5000 cm^{-1} higher in energy than the near-degenerate d_{xz} and d_{yz} orbitals, the positive VTMCD band at 38 900 cm^{-1} is assigned to the *z*-polarized, $S(p_{pseudo\ \sigma}) \rightarrow Fe(d_z2)$ $\sigma \rightarrow \sigma^*$ transition. These assignments are tentative at present and require further assessment using DFT calculations, coupled detailed VHVT MCD saturation magnetization studies to assess transition polarizations.

XAS. Figure 16 shows the iron K near-edge spectra of recombinant *P. furiosus* SOR in air-oxidized, dithionite-reduced, and (incompletely) photoreduced forms. Oxidized SOR is unusually sensitive to photoreduction, showing detectable changes in the near-edge spectrum after only one 37-min scan; the spectrum in Figure 16 is the result of exposure to the X-ray beam for 4.5 h. In contrast, the spectrum of dithionite-reduced SOR did not change on exposure to the X-ray beam (not illustrated). Fitting a linear combination of the air-oxidized and

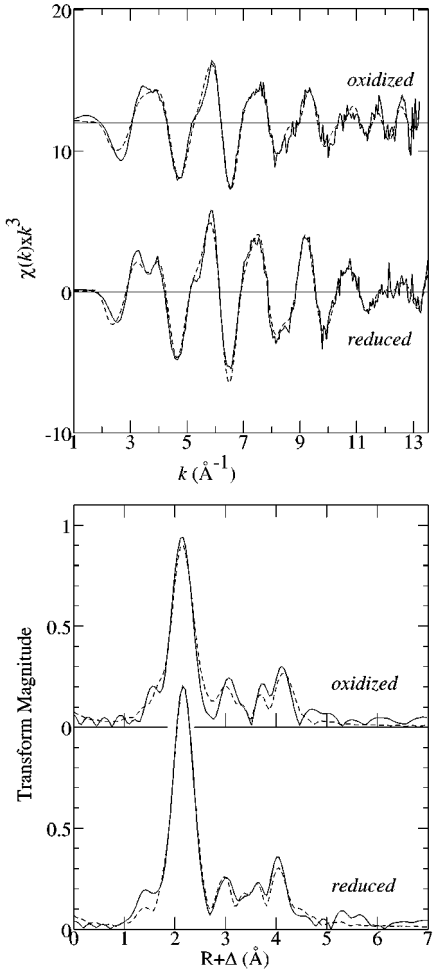

Figure 17. EXAFS oscillations (upper panel) and EXAFS Fourier transforms (lower panel) of air-oxidized and dithionite-reduced *P. furisous* SOR. Samples are described in Figure 16. The Fourier transforms are phase-corrected for Fe−N backscattering. The solid lines show experimental data while the broken lines show the results of curve-fitting analysis (Table 3).

dithionite-reduced near-edge spectra reproduced the photoreduced data sets exactly (not illustrated). This indicates that photoreduced and dithionite-reduced SOR are essentially identical with respect to the iron site, and analysis indicated first-order kinetics for the photoreduction with $k = 2.17 \times 10^{-2}$ min^{-1} (Figure 16). For the near-edge spectra, single scans provide adequate signal-to-noise ratios for our purposes, but for EXAFS spectra, averaging is required. The oxidized EXAFS data set was collected by moving the sample in the X-ray beam to interrogate a fresh spot with each scan. The near-edge and EXAFS spectra of all individual scans were compared and were found to be identical within the noise. In this way, an average XAS data set for oxidized SOR containing no more than 10% photoreduced enzyme was accumulated.

The EXAFS spectra of air-oxidized and dithionite-reduced SOR, together with the EXAFS Fourier transforms, are shown in Figure 17. The results of curve-fitting analysis are also shown in Figure 17, and the parameters for the best fits given in Table 3. Based on the crystal structure, the first shell was modeled with four nitrogen (histidine) ligands and one oxygen, plus a single sulfur. We note that EXAFS analysis cannot readily distinguish between backscatterers of similar atomic number, such nitrogen and oxygen. The outer-shell Fourier transform

Table 3. EXAFS Curve-Fitting Results for Air-Oxidized and Dithionite-Reduced *P. furiosus* SOR[a]

		Fe–N/O			Fe–S				
		N	*R* (Å)	σ^2 (Å^2)	*N*	*R* (Å)	σ^2 (Å^2)	ΔE_0	F[b]
oxidized	Fe−N/O	5	2.124(3)	0.0094(4)	1	2.361(5)	0.0065(5)	−9.8(1)	0.334
oxidized	Fe−N	2	2.072(9)[c]	0.0067(3)[d]	1	2.361(5)	0.0066(8)	−9.8(1)	0.335
	Fe−N	2	2.172[c]	0.0070[d]					
	Fe−O	1	2.150(11)	0.0069[d]					
reduced	Fe−N/O	4	2.146(2)	0.0045(2)	1	2.368(2)	0.0026(2)	−9.8(1)	0.239

[a] *N* are the coordination numbers, *R* the interatomic distances (in Å), and σ^2 the mean-square deviations in *R* (the Debye−Waller factor) (in Å^2). The values in parentheses are the estimated standard deviations (precisions) obtained from the diagonal elements of the covariance matrix. We note that the accuracies will always be larger than and related to the precisions; *R* is expected to be better than ±0.02 Å. [b] The fit error *F* is defined as $\sum[k^6(\chi_{exptl} - \chi_{calcd})^2/\sum k^6\chi_{exptl}^2]^{1/2}$. [c] Bond lengths were constrained to differ by at least 0.1 Å and at most 0.15 Å. [d] The Fe−N and Fe−O σ^2 values were constrained to be proportional to the individual bond lengths.

peaks between 3 and 4 Å are due to backscattering from the outer-shell carbons and nitrogen of the histidine ligands, and these were modeled using the approach of Poiarkova and Rehr.[36]

Curve-fitting analysis of the EXAFS of the oxidized sample thus indicated five nitrogen and oxygen ligands at 2.12 Å and one sulfur at 2.36 Å. Attempts to resolve Fe−N and Fe−O ligands did not converge to significantly different bond lengths. However, the Debye−Waller factor for the Fe−N/O ligand is unusually large at 0.0094 Å^2. The Debye−Waller factor is composed of both static and vibrational components: $\sigma^2 = \sigma^2_{stat} + \sigma^2_{vib}$. Assuming an Fe−N stretch of 220 cm^{-1}, we can compute $\sigma^2_{vb} = 0.0049$ Å,[2,36] and the EXAFS-derived Debye−Waller factor thus indicates a significant distribution in Fe−N and Fe−O bond lengths. The low-temperature high-resolution crystal structure shows two sites that resemble the oxidized EXAFS data (sites A and C)[8] and using the Fe−N and Fe−O bond lengths of these we compute $\sigma^2_{stat} = 0.0031$, which combine to give a σ^2 value of 0.008 Å^2, which is reasonably close to the EXAFS-derived value of 0.0094 ± 0.004 Å^2 (Table 3). Modeling the Fe−N/O EXAFS using three different components was attempted, using two different sets of two Fe−N interactions, plus an Fe−O interaction. The two different Fe−N components were constrained to differ by at least 0.1 Å and at most 0.15 Å, and the σ^2 values were linked to the individual bond lengths. This resulted in a fit that was not significantly better or worse than using a single Fe−N/O component (fit errors of 0.335 and 0.334, respectively), indicating that the data are at least consistent with a model of the active site that shows axial compression along one N−Fe−N axis, although direct support from EXAFS is not available.

As noted above, the low-temperature, high-resolution crystal structure of oxidized SOR shows four sites, two of which (sites A and C) are six coordinate, while the other two (B and D) are five coordinate.[8] The EXAFS-derived Fe−N/O bond length is very close to the crystallographic average bond length for sites A and C of 2.10 Å, but the Fe−S bond length of 2.36 Å is significantly shorter than the crystallographically derived value of 2.46 Å (for sites A and C). A search of the Cambridge Structure Database[37] for compounds with $Fe(N/O)_5S_1$ coordination, and excluding entries where the sulfur bridges between metals, gave an average Fe−S bond length of 2.34 Å in excellent agreement with the EXAFS-derived value. The crystal structure of sites B and D give an Fe−S bond length of 2.67 Å. A search of the Cambridge Structure Database[37] for compounds with Fe−S bond lengths greater than 2.6 Å (restricted to two-coordinate sulfur) revealed only six entries, all of which were ferrous species. Thus, while the crystallograhic Fe−S bond lengths for sites B and D are unexpected, they are not without chemical precedence.

The reduced EXAFS data fit best to a first-shell coordination of $Fe(N/O)_4S_1$ with Fe−N and Fe−S bond lengths of 2.15 and 2.37 Å, respectively. This is in agreement with the crystallographic analysis, which indicated a five-coordinate species with four histidines and one cysteine coordinated to the metal.[8] For the reduced data set, the Fe−N Debye−Waller factor is smaller that for the oxidized at 0.0045 Å^2 and is close to the vibrational value discussed above. This indicates much less static disorder in individual Fe−N distances in the reduced site than the oxidized site. As for the oxidized enzyme, the crystallographic analyses of sites A and C are in reasonable agreement with the EXAFS, while B and D appear anomalous. Thus, for A and C, the average crystallographic Fe−N and Fe−S distances are 2.12 and 2.42 Å, respectively, while for B and D, the Fe−N and Fe−S bond lengths are 2.4 and 2.7 Å, respectively. However, the crystallographically determined metal−ligand distances for sites B and D were not considered reliable due to the partial Fe occupancies (∼20%)[8] and will not be considered further. Loss of up to 50% of the active-site Fe on exposure to high concentrations of dithionite (>100-fold stoichiometric excess for 30 min) has since been confirmed by VTMCD studies of reduced samples and absorption studies of reoxidized samples (data not shown).

We conclude that the EXAFS of both oxidized and reduced enzyme confirms the crystal structures for sites A and C but that the crystal structures determined for sites B and D are not representative of the active-site structure in frozen solution. Crystallographic data collection from the oxidized sample was conducted on SSRL's beam line 9-1 and involved ∼45 min of exposure to the X-ray beam. Beam line 9-1 has ∼200-fold greater photon flux at the sample than beam line 7-3 (where the XAS data were collected), although a photon energy with ∼6-fold lower absorption cross section was used for the crystallography. The effective radiation dose rate in the crystallography experiment was thus ∼30 times that of the XAS, but for a fifth of the time. Furthermore, the crystallography was conducted at the relatively high temperature of 90 K. All of these factors will contribute toward X-ray photoreduction of the metal site. The observation that sites B and D are more sensitive to both photoreduction and reductive degradation than sites A and C suggests heterogeneity in the active-site structures at least in the crystalline state.

(36) Poiarkova, A. V.; Rehr, J. J. *Phys. Rev.* **1999**, *B59*, 948−957.
(37) Allen, F. H.; Kennard, O. *Chem. Des. Autom. News* **1993**, *1*, 31−37.

Discussion

Homologues of *P. furiosus* SOR are found in the genomes of all strict anaerobes.[2] Hence, the *P. furiosus* SOR active site is likely to represent a common strategy for oxygen detoxification in anaerobic microorganisms. The spectroscopic studies reported herein have provided detailed assessment of the ground- and excited-state electronic properties and ground-state structural information for oxidized and reduced forms of this new type of mononuclear Fe active site in solution. The results permit rationalization of apparent differences in spectroscopic properties, facilitate reconciliation of X-ray crystal structures with solution structures, and provide evidence for exogenous ligand binding at the Fe center in both the oxidized and reduced states. Each of these aspects, together with their implications for the catalytic mechanism and the role of the axial cysteine ligand, is discussed separately below.

Three subclasses of enzymes containing the SOR active site have been characterized thus far. In each case, the residues ligating the mononuclear Fe active site are rigorously conserved. The simplest are the low molecular weight proteins (subunit $M_r \sim 14.5$ kDa), initially termed neelaredoxins due to their intense blue color, which have been purified to homogeneity from *D. gigas*,[6] *P. furiosus*,[2] and *Archaeoglobus fulgidus*.[38] While neelaredoxin from *D. gigas* was originally reported to contain two Fe atoms per monomer,[6] the crystallographic and analytical studies of the highly homologous *P. furiosus* protein have shown it to contain one active-site Fe center per monomer.[2,8] Compared to these proteins, Desulfoferrodoxins (subunit $M_r \sim 14$ kDa) have an ~30-residue N-terminal extension with high sequence homology to desulforedoxin and containing four cysteine residues which ligate a rubredoxin-type Fe center. The neelaredoxin-type domain is highly conserved with a truncated C-terminus as well as 7-residue and 20-residue deletions compared to neelaredoxins. In addition to the crystallographically defined protein from *D. desulfuricans*,[9−11] Dfxs have been purified and characterized from two other sulfate-reducing bacteria, *D. vulgaris*[10,12,14,15] and *Ds. baarsii*,[3,16] and are known to be present in at least two archaea, *A. fulgidus* and *Methanobacterium thermoautotrophicum*, based on sequence considerations. The third subclass corresponds to the enzyme from *T. pallidum*,[4,5] which has high sequence homology to Dfxs, but lacks the rubredoxin-type Fe center and three of the four conserved cysteine residues in the N-terminal desulforedoxin domain.

On the basis of the UV/visible absorption and redox properties, the oxidized SOR active sites appear to be very similar in all three subclasses. However, marked differences in EPR properties have been reported. Axial $S = {}^5/_2$ resonances analogous to that reported herein for *P. furiosus* SOR ($E/D \sim 0.06$) have been observed in *D. gigas* and *A. fulgidus* neelaredoxins,[6,38] although a $g = 4.3$ feature from a rhombic ($E/D \sim 0.33$) $S = {}^5/_2$ component dominates the spectrum in the latter case. In *T. pallidum* SOR[4,5] and the Dfx proteins from sulfate-reducing bacteria,[3,11,12,15] a rhombic component ($E/D = 0.27-0.33$) has been attributed to the oxidized resting SOR active site. These apparent inconsistencies can be at least partially reconciled by the EPR studies of *P. furiosus* SOR reported herein. In the most active preparations of *P. furiosus* SOR, the axial species ($D = -0.5$ cm^{-1}, $E/D \sim 0.06$) has been shown to account for ~80% of the Fe and to exhibit a redox potential ($E_m = +250 \pm 20$ mV) in accord with that determined by optical redox titrations at room temperature ($E_m = +238 \pm 10$ mV). Moreover, by comparing native, reconstituted, and recombinant enzymes, enzymatic activity has been correlated with this axial $S = {}^5/_2$ Fe^{3+} EPR resonance and oxidation with ferricyanide has been found to result in a rhombic $S = {}^5/_2$ species attributed to a ferrocyanide-bound form. Due to the high Fe^{3+}/Fe^{2+} midpoint potential, ferricyanide has been used as an oxidant in almost all the published EPR studies. Consequently, it is possible that the rhombic $S = {}^5/_2$ species observed in *T. pallidum* SOR and the Dfx proteins are artifacts of ferricyanide oxidation and do not correspond to the functional conformation of the oxidized resting enzyme. Recent studies of *T. pallidum* SOR provide support for this hypothesis. EPR studies of hexachloroiridate-oxidized *T. pallidum* SOR revealed that 90% of Fe was present as the ($D = -0.5$ cm^{-1}, $E/D \sim 0.06$) $S = {}^5/_2$ Fe^{3+} species, with the remaining 10% contributing a rhombic $g = 4.3$ signal attributable to adventitiously bound Fe^{3+} species.[39] The existence of an axial $E/D \sim 0.06$ $S = {}^5/_2$ Fe^{3+} SOR active-site species in Dfx proteins is difficult to assess by EPR, due to overlap with resonance from the desulforedoxin $S = {}^5/_2$ Fe^{3+} center ($D > 0$, $E/D = 0.08$). However, Mössbauer studies of *D. desulfuricans* Dfx argue strongly in favor of a homogeneous, rhombic $S = {}^5/_2$ ground state ($E/D = 0.28$, $D = -1.4$ cm^{-1}) for the oxidized SOR site (center II), even in the absence of exogenous ligands or oxidants.[11] This suggests a different active-site conformation for the oxidized SOR center in Dfx. It remains to be determined if this rhombic species corresponds to a functional conformation or if conditions can be found in Dfx to effect conversion to the axial species that is associated with the most active form of monoiron SORs

The X-ray crystal structures of *P. furiosus* SOR (oxidized and reduced)[8] and *D. desulfuricans* Dfx (oxidized)[9] have both revealed an SOR active site comprising a mononuclear Fe coordinated by the imidazole nitrogens of four equatorial histidines (three ϵN and one δN) and one apical cysteinyl sulfur. However, the ligation and coordination number of the oxidized Fe center was not fully resolved by the crystal structures. In two of the four subunits of *P. furiosus* SOR, a conserved glutamate carboxylate serves as the sixth ligand, while in the other two subunits and in *D. desulfuricans* Dfx, the sixth coordination site is vacant or occupied by a weakly coordinated solvent molecule. After reduction of crystalline *P. furiosus* SOR with a large excess of dithionite, two of the Fe sites showed only partial occupancy (~20%) and the other two exhibited square-pyramidal Fe sites with no indication of a solvent molecule at the vacant coordination site.

In light of the photoreduction observed in XAS studies of oxidized *P. furiosus* SOR, it seems very likely that the discrepancies in oxidized crystal structures reflect partial (*P. furiosus* SOR) or complete (*D. desulfuricans* Dfx) photoreduction by the synchrotron radiation to yield a reduced SOR active site with square-pyramidal coordination geometry. Furthermore, the electronic properties of the oxidized high-spin Fe^{3+} center in active *P. furiosus* SOR, as deduced by EPR and VTMCD, are consistent with the glutamate-bound structure. The ground-state zero-field splitting parameters, $D = -0.5$ cm^{-1} and E/D

(38) Abreu, I. A.; Saraiva, L. M.; Carita, J.; Huber, H.; Stetter, K. O.; Cabelli, D. E.; Teixeira, M. *Mol. Microbiol.* **2000**, *38*, 322−334.

(39) Clay, M. D.; Rusnak, F. M.; Johnson, M. K., unpublished results.

$\sim$ 0.06, indicate an octahedrally ligated Fe^{3+} center with a predominantly axial compression.[33] The transition polarizations for the S-to-Fe^{3+} CT bands deduced from VHVT MCD saturation magnetization studies dictate that the compression (zero-field-splitting) axis is perpendicular to the Fe−S axis. Hence, the strong field axis is along one of the N−Fe−N axes, which is in accord with imidazole generally being a stronger field ligand than thiolate or carboxylate. In addition, the low-temperature crystallographic data for *P. furiosus* SOR indicate that the two N−Fe−N axes are not equivalent; the average Fe−N distances for one pair of trans His ligands (2.09 Å for His16(ϵN) and His47(ϵN)) $\sim$0.1 Å shorter than the other pair (2.19 Å for His41(ϵN) and His114(δN)).[8] The strong-field axis is, therefore, defined by His16 and His47, and the crystallographic data indicate that this axis lies within the Fe−S−C plane, in accord with the axis system used in making electronic assignments (see Figure 8).

The EXAFS data for oxidized *P. furiosus* SOR, one Fe−S at 2.33 Å and an Fe−N/O shell that can be fit equally well to five Fe−N/O at 2.12 Å or two Fe−N at 2.07 Å, two Fe−N at 2.17 Å, and one Fe−O at 2.15 Å, are also in good agreement with crystallographic data for the six-coordinate glutamate-bound form. The major difference lies in a shorter Fe−S distance (2.36 Å from the EXAFS data compared to 2.46 Å for the two glutamate-ligated sites in the crystal structure[8]). A long Fe−S distance of 2.46 Å is also incompatible with the strong pπ−dπ S−Fe interaction that is evident from analysis of the excited-state properties. While both the EXAFS and electronic properties are consistent with a distorted octahedral Fe^{3+} site in oxidized SOR, neither can specifically address the identity of the sixth ligand. However, the crystallographic data for *P. furiosus* SOR,[8] coupled with the recent mutagenesis results for *D. vulgaris* and *Ds. baarsii* Dfx,[14,16] which reported an $\sim$60-nm blue shift in the visible absorption S-to-Fe^{3+} CT band in variants in which the conserved glutamate residue was replaced by alanine, strongly support the monodentate glutamate carboxylate as the sixth ligand to the oxidized Fe site in all three subclasses of SOR.

Near-IR VTMCD studies of reduced *P. furiosus* SOR have confirmed that the square-pyramidal Fe coordination evident in the reduced crystal structure persists in solution. The large splitting in the near-IR ligand field transitions, $\Delta^5E_g > 7400$ cm^{-1}, dictates a large separation in the $d_{x^2-y^2}$ and d_{z^2} orbitals, suggesting a weak axial ligand with the Fe not far removed from the equatorial plane.[27] This is in good agreement with the crystallographic data, which positions the Fe at an angle of $\sim$12° above the plane of the four ligated N atoms. On the basis of purely geometric considerations, this square-pyramidal ligand field would be expected to result in $D < 0$, i.e., the t_{2g} set of orbitals split with d_{xz} and d_{yz} nearly degenerate and lower in energy than d_{xy}. The observed inversion of this splitting pattern, as evidenced by $D > 0$, could be rationalized in terms of a strong axial ligand such that the Fe is extensively pulled out of the equatorial plane or covalency effects such as π interaction between the S p_π and $p_{\text{pseudo }\sigma}$ orbitals and the Fe d_{xz} and d_{yz} orbitals. The large splitting in the e_g set of orbitals coupled with the crystallographic data and the UV VTMCD/absorption evidence for $\pi \rightarrow \pi^*$ $(Cys)S^- \rightarrow Fe^{2+}$ CT transitions therefore indicates that the positive axial zero-field splitting observed in reduced SOR is a result of significant pπ−dπ Fe−S interaction. EXAFS of the reduced enzyme also agrees well with the reduced crystal structure with 4 Fe−N at 2.15 Å and one Fe−S at 2.37 Å. The Fe−S distance is significantly shorter than the average of the two crystallographically defined distances, 2.42 Å, but is consistent with the pπ−dπ Fe−S interaction that is required to rationalize the ground-state and excited-state electronic properties.

The opposite signs of the near-IR VTMCD ligand field bands of reduced SOR provide information on the nature of the active-site distortion from idealized square-pyramidal coordination geometry. In the majority of square-pyramidal Fe^{2+} inorganic complexes investigated thus far, both near-IR ligand field VTMCD bands are positively signed.[40] Opposite signs require a low-symmetry point group in which the $d_{x^2-y^2}$ and d_{z^2} orbitals transform as different irreducible representations. This can occur under C_s symmetry for the SOR active site, provided the mirror plane bisects rather than contains the Fe−N bonds. In agreement with this prediction, inspection of the active-site crystal structure, including the imidazole rings of the coordinated histidines, does reveal an approximate mirror plane bisecting the His114 and His47 Fe−N bonds.

The spectroscopic studies reported in this work demonstrate that the *P. furiosus* SOR active site is accessible for exogenous ligand binding in both the oxidized and reduced states. Evidence has been presented for azide, hydroxide, ferrocyanide, and cyanide binding to the Fe^{3+} site in place of the glutamate carboxylate. Cyanide binding induces a high-spin to low-spin transition and has afforded detailed insight into the ground- and excited-state electronic properties of a low-spin Fe^{3+} derivative of SOR. Azide, hydroxide, and ferricyanide binding occur with retention of the high-spin electronic configuration and are manifest by a change from a predominantly axial to a near-rhombic $S = {}^5/_2$ ground state. More work is required to establish definite evidence for hydroxide and ferrocyanide binding. The alkaline transition, $pK_a = 9.6$, which has been observed in *D. gigas* neelaredoxin[6] and *P. furiosus* SOR, has been attributed to hydroxide displacing the glutamate ligand, on the basis of the VTMCD studies that indicate that the same pattern of $(Cys)S^- \rightarrow Fe^{3+}$ and π His $\rightarrow Fe^{3+}$ CT bands each blue-shifted by $\sim$1500 cm^{-1}. This implies that the histidyl and cysteinyl ligation is retained and the blue shift in the CT bands is consistent with hydroxide binding and a concomitant increase in electron density at the Fe site. Ferrocyanide binding appears to be the most reasonable explanation of the "azide-like" changes in the ground-state properties that are induced on ferricyanide oxidation. Near-IR VTMCD studies have provided compelling evidence for azide and cyanide binding at the vacant coordination site of the square-pyramidal ferrous active site of reduced *P. furiosus* SOR. Azide binds weakly with a coordination geometry intermediate between octahedral and square pyramidal, whereas cyanide binds to give an octahedrally ligated high-spin ferrous derivative.

The ability to bind exogenous ligands to both the ferric and ferrous active sites is consistent with an inner-sphere mechanism for superoxide reduction. The most plausible, albeit unproven, mechanism involves superoxide binding at the vacant coordination site of reduced SOR coupled with electron transfer from iron to superoxide to yield ferric−peroxo, ferric−hydroperoxo,

(40) Pavel, E. G.; Kitajima, H.; Solomon, E. I. *J. Am. Chem. Soc.* **1998**, *120*, 3949−3962.

or both intermediates. Under this scenario, the cysteine, which is trans to the superoxide binding site, would play a crucial role in pushing electron density on to the iron in order to promote ferrous-to-superoxide electron transfer, product dissociation from the ferric−(hydro)peroxo intermediate, or both. Hence, the strong pπ−dπ Fe−S bonding interactions that have been identified in this study in both the oxidized and reduced forms of SOR are likely to provide an important electronic contribution to active-site reactivity. In addition, by analogy with blue copper proteins,[41] the pπ−dπ Fe−S bonding interaction in SOR may provide a superexchange pathway to facilitate electron transfer from rubredoxin.

Recent pulse radiolysis kinetic studies of Dfx from *D. vulgaris*[14] and *D. baarsi*[16] and SOR from *T. pallidum*[17] have facilitated characterization of the visible absorption spectra of transient intermediates in the catalytic mechanism of superoxide reduction. While the results of these studies are not in good agreement, it is appropriate to evaluate the published interpretations in light of the detailed assessment of the electronic properties presented herein. The study of *D. vulgaris* Dfx reported a transient intermediate, characterized by a visible absorption band at 600 nm (16 700 cm^{-1}), that appears as a result of a bimolecular reaction occurring at a nearly diffusion-controlled rate, 1.5×10^9 M^{-1} s^{-1}, and disappears in a slower unimolecular reaction with a rate of 40 s^{-1}. By analogy with the optical properties of ferric−(hydro)peroxo complexes,[33] this absorption band was attributed to the (hydro)peroxo-to-ferric CT band of a putative ferric (hydro)peroxo intermediate. However, since the hydroxide-bound form of oxidized *P. furiosus* SOR and the E47A variant of *D. vulgaris* Dfx[14] both exhibit intense absorption bands at 600 nm that arise exclusively from cysteinyl-S-to-ferric CT transitions, assignment to a (hydro)peroxo-to-ferric CT band may be premature at this stage. It is also important to note that the hydroperoxo-to-ferric CT band in activated bleomycin,[33,42] as well as a wide range of related end-on, low-spin ferric hydroperoxy complexes,[43] has weak absorption intensity compared to that of the intense cysteinyl-S-to-ferric CT transitions seen in SOR.

The results and interpretation of the kinetic study of *Ds. baarsii*[16] are more perplexing. Two intermediates were identified. The first forms rapidly as a result of a bimolecular reaction at near diffusion-controlled rates, 1.1×10^9 M^{-1} s^{-1}, and is characterized by intense visible absorption bands at 550 nm (18 200 cm^{-1}) and 610 nm (16 400 cm^{-1}). Without explanation, this intermediate was tentatively attributed to a ferrous−superoxide species. Although the possibility that one or both of these bands arises from an unprecedented ferrous-to-superoxide CT transition cannot be completely discounted, assigning these transitions to a ferrous species is considered extremely unlikely in light of the visible absorption properties of the ferrous and ferric SOR derivatives investigated in this work. The initial intermediate is reported to decay to a second intermediate in a unimolecular reaction with a rate of 500 s^{-1}. This intermediate is characterized by an intense absorption band at 630 nm (15 900 cm^{-1}) that was attributed to the peroxo-to-ferric CT band of a ferric−(hydro)peroxo species. However, assignment of this species as catalytic intermediate must be viewed as questionable at this stage. The visible absorption properties deduced for this intermediate are very similar to those of the oxidized SOR center in this enzyme (absorption maximum at 644 nm, 15 500 cm^{-1}), and the absorption spectrum of the final species was not determined. Even if it does correspond to an intermediate, we conclude that the 630-nm absorption band is more likely to be result from cysteinyl-S-to-ferric CT than peroxo-to-ferric CT.

Optical absorption changes during pulse radiolysis studies of *T. pallidum* SOR are easier to assess than in Dfx due to the absence of the additional rubredoxin-type iron center. Two intermediates were identified.[17] The first was formed at near diffusion-controlled rates, 6×10^8 M^{-1} s^{-1}, and is characterized by a visible absorption band centered near 610 nm (16 400 cm^{-1}). This decays in a slower step, 4800 s^{-1}, to yield a second intermediate exhibiting an absorption band at 670 nm (14 900 cm^{-1}). The first and second intermediates were assigned to ferric−peroxo and ferric−hydroperoxo species, respectively, with the visible absorption bands attributed to peroxo-to-ferric and hydroperoxo-to-ferric CT transitions, respectively. However, this assignment is not consistent with the energies of the observed CT bands. Peroxo-to-ferric CT is predicted to occur at *lower* energy than hydroperoxo-to-ferric CT in the absence of other changes in iron coordination geometry or ligation. This prediction has been verified experimentally in the only model complex for which both ferric−peroxo and ferric−hydroperoxo forms have been characterized. Protonation of the side-on peroxo ligand (η^2-O_2^{2-}) in [(trispicMeen)Fe(O_2)]$^+$ to yield the end-on hydroperoxo complex [(trispicMeen)Fe(OOH)]$^{2+}$ is marked by a dramatic blue shift in the visible CT band from 740 (13 500 cm^{-1}) to 540 nm (18 500 cm^{-1}).[44] Ironically, the published assignment for the two intermediate species identified in *T. pallidum* SOR[17] is quite reasonable provided the observed visible CT bands are assigned to cysteinyl-S-to-ferric CT rather than (hydro)peroxo-to-ferric CT. Protonation of the ligand trans to cysteine would be expected to shift the cysteinyl S-to-ferric CT to lower energy as observed. Hence, the published interpretation may be correct, albeit for the wrong reasons.

In summary, the three kinetic studies of the SOR mechanism reported thus far do not concur and none has provided compelling spectroscopic evidence for a putative ferric−peroxy or ferric−hydroperoxy intermediate. The observed changes in the energy of visible charge-transfer band are best interpreted in terms of changes in the energy of the cysteinyl-S-to-ferric CT transition that are induced by changes in the trans ligand rather than the appearance of intense (hydro)peroxo-to-ferric CT bands. We conclude that there is still much to be learned about the catalytic mechanism of SOR and that understanding the electronic transitions associated with the cysteine ligand will be crucial in this endeavor. The present study has provided a detailed understanding of the structural, electronic, magnetic, and ligand binding properties of the mononuclear iron active site in wild-type SOR. In addition to providing insight into the electronic properties and bonding of a unique non-heme iron active site with a single cysteine ligand, the results set the stage for future kinetic, mutagenesis, and spectroscopic studies designed to elucidate the catalytic mechanism and the role of

(41) Lowery, M. D.; Guckert, J. A.; Gebhard, M. S.; Solomon, E. I. *J. Am. Chem. Soc.* **1993**, *115*, 3012−3013.
(42) Neese, F.; Zaleski, J. M.; Loeb Zaleski, K.; Solomon, E. I. *J. Am. Chem. Soc.* **2000**, *122*, 11703−11724.
(43) Girerd, J.-J.; Banse, F.; Simaan, A. J. *Struct. Bonding* **2000**, *97*, 145−177.
(44) Simaan, A. J.; Banse, F.; Mialan, P.; Bousac, A.; Un, S.; Kargar-Grisel, T.; Bouchoux, G.; Girerd, J.-J. *Eur. J. Inorg. Chem.* **1999**, 993−996.

key residues in optimizing the active site for superoxide reduction as opposed to dismutation.

Acknowledgment. This work was supported by grants from the National Institutes of Health (GM60329 to M.W.W.A and M.K.J.) and a National Science Foundation Research Training Group Award to the Center for Metalloenzyme Studies (DBI9413236). Work at SSRL was funded by the Department of Energy, Offices of Basic Energy Sciences and Biological and Environmental Research, and the National Institutes of Health (RR01209). We thank Professor E. I. Solomon and Dr. Frank Neese for supplying the programs used in analyzing VHVT MCD magnetization data and for stimulating discussions.

Supporting Information Available: Redox titration of *P. furiosus* SOR at pH 7.0 as monitored by UV/visible absorption at 660 nm (Figure S1) and the effect of pH on the visible absorption maximum of *P. furiosus* SOR (Figure S2). See any current masthead page for ordering information and Web access instructions.

JA016889G